

Characterization of starspots on a young M-dwarf K2-25: multi-band observations of stellar photometric variability and planetary transits

Mayuko Mori,^{1*} Kai Ikuta,¹ Akihiko Fukui,^{2,3} Norio Narita,^{2,3,4} Jerome P. de Leon,¹ John H. Livingston,^{4,5,6} Masahiro Ikoma,⁷ Yugo Kawai,¹ Kiyoe Kawauchi,⁸ Felipe Murgas,^{3,9} Enric Pallé,^{3,9} Hannu Parviainen,^{3,9} Gareb Fernández Rodríguez,^{3,9} Yuka Terada,^{10,11} Noriharu Watanabe,¹ Motohide Tamura^{4,5,12}

¹Department of Multi-Disciplinary Sciences, Graduate School of Arts and Sciences, The University of Tokyo, 3-8-1 Komaba, Meguro, Tokyo 153-8902, Japan

²Komaba Institute for Science, The University of Tokyo, 3-8-1 Komaba, Meguro, Tokyo 153-8902, Japan

³Instituto de Astrofísica de Canarias (IAC), 38205 La Laguna, Tenerife, Spain

⁴Astrobiology Center, 2-21-1 Osawa, Mitaka, Tokyo 181-8588, Japan

⁵National Astronomical Observatory of Japan, 2-21-1 Osawa, Mitaka, Tokyo 181-8588, Japan

⁶Department of Astronomy, School of Science, The Graduate University for Advanced Studies (SOKENDAI), 2-21-1 Osawa, Mitaka, Tokyo, Japan

⁷Division of Science, National Astronomical Observatory of Japan, 2-21-1 Osawa, Mitaka, Tokyo 181-8588, Japan

⁸Department of Physical Sciences, Ritsumeikan University, Kusatsu, Shiga 525-8577, Japan

⁹Departamento de Astrofísica, Universidad de La Laguna (ULL), 38206 La Laguna, Tenerife, Spain

¹⁰Institute of Astronomy and Astrophysics, Academia Sinica, P.O. Box 23-141, Taipei 10617, Taiwan, R.O.C.

¹¹Department of Astrophysics, National Taiwan University, Taipei 10617, Taiwan, R.O.C.

¹²Department of Astronomy, Graduate School of Science, The University of Tokyo, 7-3-1 Hongo, Bunkyo, Tokyo 113-0033, Japan

Accepted 2024 March 20. Received 2024 March 19; in original form 2024 February 12

ABSTRACT

Detailed atmospheric characterization of exoplanets by transmission spectroscopy requires careful consideration of stellar surface inhomogeneities induced by starspots. This effect is particularly problematic for planetary systems around M-dwarfs, and their spot properties are not fully understood. We investigated the stellar activity of the young M-dwarf K2-25 and its effect on transit observations of the sub-Neptune K2-25 b. From multi-band monitoring observations of stellar brightness variability using ground-based telescopes and TESS, we found that the temperature difference between the spots and photosphere is < 190 K and the spot covering fraction is $< 61\%$ (2σ). We also investigated the effect of starspot activity using multi-epoch, multi-band transit observations. We rule out cases with extremely low spot temperatures and large spot covering fractions. The results suggest that spots could distort the transmission spectrum of K2-25 b by as much as ~ 100 ppm amplitude, corresponding to the precision of JWST/NIRSPEC of the target. Our study demonstrates that simultaneous multi-band observations with current instruments can constrain the spot properties of M-dwarfs with good enough precision to support atmospheric studies of young M-dwarf planets via transmission spectroscopy.

Key words: stars: starspots – planets and satellites: atmospheres – planets and satellites: individual: K2-25 b – techniques: photometric

1 INTRODUCTION

The number of discovered exoplanets now exceeds 5000, largely due to space-based transit surveys, such as the Kepler space telescope (Borucki et al. 2010) and the Transiting Exoplanets Survey Satellite (TESS; Ricker et al. 2015). Among the various planetary groups, planets feasible for transmission spectroscopy are one of the most interesting targets to characterize their atmospheres. The James Webb Space Telescope (JWST; Gardner et al. 2006) and future space telescopes such as Ariel (Tinetti et al. 2018, 2021), with their extremely

high precision, enable us to detect atmospheric signals of less than 100 ppm, which allows more detailed analysis of the planetary atmospheric compositions.

Recently, the transit light source effect (TLSE) has been identified as a significant factor affecting planetary transmission spectra (Rackham et al. 2018, 2023). In brief, unocculted spots or faculae during planetary transits make the observed transit depth shallower or deeper than the expected transit depth without spots or faculae. This effect is particularly complicated for the planets around active M-dwarfs: the wavelength dependence of this effect is confounded by the absorption of molecules present in both stellar photosphere and spots, resulting in false positive signals of planetary atmospheres.

* E-mail: mayukomori.519@gmail.com

Some studies have investigated the possibility that signals in transmission spectra can be interpreted as either due to planetary atmospheres or TLSE (e.g., [Edwards et al. 2021](#); [Gressier et al. 2022](#); [Barclay et al. 2021](#); [Moran et al. 2023](#)).

In atmospheric retrievals of exoplanet spectra, it is common practice to make empirical assumptions about the stellar surface models, which are specified in spot temperatures and covering fractions (the ratio of projected spot area to the stellar disk) (e.g., [Pinhas et al. 2018](#); [Cracchiolo et al. 2021](#)). In other cases, it is common to optimize transmission spectra by atmosphere models and stellar surface models simultaneously (e.g., [Lim et al. 2023](#); [Fournier-Tondreau et al. 2024](#)). However, many degeneracies between stellar surface and planetary atmospheric models make it challenging to assume/retrieve realistic stellar surface models ([Rackham & de Wit 2023](#); [Berardo et al. 2023](#)). In addition, what makes the assumption of stellar surface models difficult is that the spot characteristics have not been well studied, especially for M-dwarfs. The commonly used empirical relations of spot temperature and stellar surface temperature ([Berdyugina 2005](#); [Maehara et al. 2017](#); [Herbst et al. 2021](#)) are derived mainly from observations of solar-type stars.

A useful method to constrain spot temperature is multi-band photometric observations of rotational modulation of stellar brightness caused by spots appearing and disappearing in the observed hemisphere of the star (e.g., [Henry et al. 1995](#); [Morris et al. 2018](#)). In this method, it is necessary to perform simultaneous multi-band observations because the spot distribution could be different if two observations are widely separated in time. However, there are a few studies with such observational strategies ([Rosich et al. 2020](#)) because intensive observations are required.

The purpose of this study is to investigate the spot activity of an M-dwarf and its impact on planetary transits through multi-band observations in the optical. As a target, we selected the active M-dwarf K2-25, which harbours a sub-Neptune (K2-25 b) that is a candidate for future atmospheric characterization. To derive its current spot characteristics, we performed simultaneous multi-band monitoring observations of K2-25 with ground-based telescopes concurrently with TESS. In addition, we conducted ground-based multi-band transit observations of K2-25 b to assess the effects of these spot characteristics on measurements of planetary transits.

1.1 K2-25 system

K2-25 is a young M4.5 dwarf in the Hyades cluster. Its sub-Neptune-sized planet K2-25 b was discovered by Kepler space telescopes in K2 Campaign 4 ([Mann et al. 2016](#)). The fundamental parameters of the K2-25 system are summarized in Table 1.

As K2-25 is a member of the Hyades cluster, the age of the system is well-constrained to be 650 ± 70 Myr ([Martín et al. 2018](#)). This makes possible an in-depth discussion of the formation and evolution process of the planet’s atmosphere, once observational constraints on the atmosphere are obtained. With its relatively bright host star and deep transits, the planet is a promising target for atmospheric studies with the JWST, Ariel, and next-generation telescopes.

However, the star has a brightness variability with a period of ~ 1.88 days, suggesting that it is an active star with spots. As they would affect the result of transmission spectroscopy, several previous studies have investigated the atmospheric properties of K2-25 b with the stellar activity of the host star in mind.

[Thao et al. \(2020\)](#) derived transit depths from a low-resolution transmission spectrum with multiple transit datasets obtained from several space- and ground-based telescopes. They compared the derived spectrum with atmosphere models, combined with stellar sur-

Table 1. Fundamental parameters of K2-25. The source “Gaia DR3” means the data from the Gaia mission Data Release 3 ([Gaia Collaboration et al. 2016, 2023](#)).

Parameter	Value	Source
<i>Equatorial coordinates, parallax, and proper motion</i>		
R.A. (J2000)	04 ^h 13 ^m 05.613 ^s	Gaia DR3
Dec. (J2000)	+15° 14′ 52.02″	Gaia DR3
π (mas)	22.3572 \pm 0.0308	Gaia DR3
μ_α (mas yr ⁻¹)	122.450 \pm 0.038	Gaia DR3
μ_δ (mas yr ⁻¹)	-18.603 \pm 0.026	Gaia DR3
<i>Fundamental parameters</i>		
T_{eff} (K)	3207 \pm 58	Thao et al. (2020)
[Fe/H] (dex)	0.15 \pm 0.03	Mann et al. (2016)
M_\star (M_\odot)	0.2634 \pm 0.0077	Thao et al. (2020)
R_\star (R_\odot)	0.2932 \pm 0.0093	Thao et al. (2020)
ρ_\star (g cm ⁻³)	14.7 \pm 1.5	Thao et al. (2020)
log g (cgs)	4.944 \pm 0.031	Thao et al. (2020)
distance (pc)	45.01 ^{+0.16} _{-0.17}	Thao et al. (2020)
Luminosity (L_\odot)	0.00816 \pm 0.00029	Thao et al. (2020)
Age (Gyr)	0.730 ^{+0.050} _{-0.052}	Mann et al. (2016)

face models assuming a spot temperature of 2800 K or 3000 K on a stellar surface of 3200 K. They found that the transmission spectrum of K2-25 b prefers a flat model to a clear solar-abundance atmosphere model, as a large spot covering fraction (22% or 36%) was needed to fit a solar-abundance atmosphere model, and such a large spot covering fraction contradicts the observed amplitude of brightness variations. Therefore, they concluded that, although TLSE could be at play to some extent, the atmospheric spectrum of K2-25 b is flat, which indicates a cloudy/hazy atmosphere and/or a high mean molecular weight atmosphere.

[Gaidos et al. \(2020\)](#) and [Stefansson et al. \(2020\)](#) measured the stellar obliquity and planetary mass via spectroscopic observations. Their radial velocity observations yielded a planetary mass higher than that expected from a mass-radius relation, making the amplitude of the atmospheric signal in the transmission spectrum smaller without necessitating the presence of clouds or hazes.

No detailed space-based transmission spectroscopy has ever been performed for K2-25, and such observations by JWST and similar instruments are needed to investigate whether the atmospheric spectrum of K2-25 b is flat. On the other hand, high-precision spectroscopy will need to pay more attention to TLSE, as it will be sensitive to small differences in spot properties, which can complicate the interpretation of atmospheric models. [Thao et al. \(2020\)](#) made empirical assumptions about spot temperatures, but more realistic stellar surface models can be constrained by observations. Interest in the K2-25 system itself and the need to understand its current spot activity are the reasons we chose this system as our target, in addition to the fact that it was a good test case for our methods.

The remainder of the paper is organized as follows: Section 2 summarizes the observational data used in our analyses; Section 3 describes our analysis methods for constraining the spot characteristics from multi-band monitoring and transit light curves; Section 4 describes K2-25’s spot characteristics and the effect of the spots on the transit observations, and compares our results with previous studies. Section 5 summarizes the results and discussions, with the future prospects of studying spot properties of M-dwarfs.

2 OBSERVATIONS & DATA REDUCTIONS

The observations are divided into two categories: monitoring photometry to investigate stellar brightness variations using TESS, Sinistro, and ZTF (Section 2.1, 2.2, and 2.3); transit photometry to evaluate the effect of spots on transit depth measurements by TESS, MuSCAT2, and MuSCAT3 (Section 2.1 and 2.4). These observations were conducted at optical wavelengths, where the spot effect is expected to be prominent. The data are summarized in Table 2.

2.1 Monitoring and transit photometry - TESS

K2-25 (TIC 434226736, TOI-5095) was observed by TESS in Sector 44 (2021 October 12 to November 6) during TESS Cycle 4 with a 2-min cadence in the TESS bandpass (600–1000 nm). We used the PDCSAP (Pre-search Data Conditioning Simple Aperture Photometry) light curves produced by the Science Processing Operations Center (SPOC) photometry pipeline (Jenkins 2002; Jenkins et al. 2010, 2016) for both the monitoring and transit analyses. We also checked the SAP (Simple Aperture Photometry-) light curves, as sometimes stellar modulation is removed from the PDCSAP light curves. We confirmed that the brightness variation on K2-25 was almost identical in the SAP and PDCSAP light curves, both in shape and normalized amplitude, with instrumental systematics and a long-term trend corrected in PDCSAP light curve. In addition, while nearby stars blending into the TESS aperture may affect photometric accuracy, we confirmed that their effects were negligible (Appendix A1).

To analyse the brightness variability, we removed outliers with more than 3σ away from the median of the normalized light curve. In the transit analyses, for the six transits observed by TESS, non-detrended light curves were cut out for a range of 0.1 days before and after the predicted transit-centre time.

2.2 Monitoring photometry - LCO 1m / Sinistro

Sinistro is a single-band optical camera mounted on five 1m telescopes worldwide, operated by Las Cumbres Observatory (LCO, Brown et al. 2013). Our observations were performed specifically with the telescopes at McDonald Observatory in Texas and at Teide Observatory in Tenerife, Canary islands. Sinistro has a $26'.5 \times 26'.5$ field of view with a pixel scale of $0.389'' \text{pix}^{-1}$.

We observed K2-25 from 2021 October 02 to November 05 with Sinistro in g -band (400–550 nm), and from 2021 October 13 to 2022 January 31 in z -band (820–920 nm). With the exposure time of 120 seconds in g -band and 40 seconds in z_s -band (denoted z -band hereafter for simplicity), 5–15 frames were taken every 4–5 hours during good observing conditions with airmass < 1.6 , moon distance > 30 deg, and no weather or instrumental issues. Data reduction was carried out through the LCO BANZAI pipeline (McCully et al. 2018). The photometry was obtained using the package `astropy-Photutils` (Bradley et al. 2021). We found that circular apertures with a radius of 8 pixels were optimal to reduce the scatter in the light curves. We also subtracted the sky background noise calculated using an annulus with a radius of 50 to 80 pixels.

We adopted the differential photometry method to account for the telluric variability. In practice, the telluric effect on stellar brightness variations should depend on the colour of the star, given that atmospheric extinction occurs to different degrees for stars of different colours. To minimise this effect, we only used stars with colours similar to the target as comparison stars. We calculated the $g - z$ colour of each star in the field of view from the catalogue of Pan-STARRS Data Release 2 (Chambers et al. 2016; Flewelling et al. 2020). As

the $g - z$ value of K2-25 is 3.48, we selected stars with $g - z > 2$ for use in the calculation.

We excluded frames with the following three conditions as outliers: (i) the number of detected stars was smaller than 50; (ii) the median stellar magnitude was > 0.7 mag fainter than that of the reference frame; (iii) the obtained target brightness was more than 3σ different from the mean model obtained by fitting a third-order polynomial.

2.3 Monitoring photometry - ZTF

The Zwicky Transient Facility (ZTF) is a time-domain survey that conducts a full sweep of the northern visible sky every two days (Bellm et al. 2019). The survey is performed by a camera with a 47 square degree field of view mounted on the Samuel Oschin 1.2m telescope at Palomar Observatory in California (Bellm et al. 2019).

We used the archival photometry of K2-25 in Z_g and Z_r -bands (367.6–561.4 and 549.8–739.4 nm), which is similar to SDSS g and r -band (Masci et al. 2019), from 2018 March 27 until 2022 March 2. For the ZTF light curves, we removed the data points with the quality warning flags (expressed as ‘catflags’ in the ZTF catalogue), and data points where zero-magnitude is 3σ away from the median value of zero-magnitude. In addition, the magnitude was corrected for the second-order extinction effect by a linear function of colour coefficients (‘clcoeff’ in the ZTF catalogue). Finally, the magnitude was converted to flux, from which we produced a normalised light curve.

We found that the shape of brightness variations of K2-25 had changed over a timescale of ~ 200 days possibly due to the variation of spot distribution (see Appendix A3). Therefore, in order to maintain simultaneous observations with the other dataset, we only used the data after MJD = 59400 (2021 July 5) in the analyses.

2.4 Transit photometry - MuSCAT2 and MuSCAT3

MuSCAT2 and MuSCAT3 are simultaneous multi-band cameras with four optical channels of g , r , i , and z -bands (400–550, 550–700, 700–820, and 820–920 nm) (Narita et al. 2019, 2020). MuSCAT2 is installed on the 1.52m Telescopio Carlos Sánchez in the Teide Observatory, Canaries, and MuSCAT3 is on 2m Faulkes Telescope North at Las Cumbres Observatory (LCO) on Haleakala, Maui. MuSCAT2 and MuSCAT3 share common features, while they are different in pixel scale ($0.44''$ and $0.27''$ for MuSCAT2 and 3) and field of view ($7'.4 \times 7'.4$ and $9'.1 \times 9'.1$).

We observed four transits of K2-25 b with MuSCAT2 on 2021 December 8, 22, 29, and 2022 January 5, and two transits with MuSCAT3 on 2022 January 8 and 29. The exposure times and number of data for each observing night are summarised in Table 2. A transit number N_T was introduced to indicate how many transits have occurred with the transit at $T_0 = 2458515.64206$ (BJD) (Stefansson et al. 2020) as the starting point. We note that the i -band camera was not available on 2021 December 8 and 22, because of technical difficulties with the instrument.

These observations were not exactly simultaneous with the TESS observations, and there was a gap of 35 days (~ 10 planetary orbital periods) between the last transit with TESS and the first transit with MuSCAT2.

The reduction for MuSCAT2 data and the aperture photometry of both MuSCAT2/3 datasets were conducted by the custom pipeline described in Fukui et al. (2011), and the reduction for MuSCAT3 data was carried out by the BANZAI pipeline. For each night and each band, the optimal aperture radius was found by selecting the value

between 8 and 14 pixels that minimized the scatter in the light curve. Between one and three stars brighter than the target were selected as comparison stars for each night and each band.

The derived raw light curves are shown in Figure A.9. Apart from the transit signal, some rapid flux increases were detected especially in shorter wavelengths, which are likely to be flares. In particular, we visually detected a significant flare-like slope in *g* and *r*-band light curves for transit $N_T = 307$. We also detected a flux bump during the transit for light curve $N_T = 314$, which might be a flare during the transit or a spot crossing.

The removal of outliers was conducted as follows. First, we removed a flux jump caused by a flare-like signal in $N_T = 307$. As the highest peak of the signal was at BJD= 2459585.36556, the data points 0.01 day before and after this timestamp were removed. Although the flare-like signal was not visually obvious in *i* and *z*-band, we removed the points in all bands to reduce the bias from arbitrary manipulation. Then, we fit each light curve at each band and each date one by one, using mean models as the transit model combined with the baseline model. The transit model was calculated by the package *batman* (Kreidberg 2015) from the transit parameters described in Section 3.6. The baseline model was defined by a third-order polynomial of time. The models were optimized using MCMC package *emcee* (Foreman-Mackey et al. 2013). We removed outliers with more than 3σ away from the mean model. We repeated this operation three times (Figure A.9).

3 ANALYSES & RESULTS

The analyses described in this section are divided into two main parts. First is the analysis of stellar brightness variability to constrain the spot characteristics and to calculate the degree of TLSE (Section 3.1 to 3.5). Second is the multi-band transit depth derivation to evaluate the TLSE (Section 3.6). Additional analyses and results are described in the Appendix.

3.1 Monitoring light curve analyses - rotation period

We obtained five light curves: the TESS light curve, Sinistro light curves in *g*- and *z*-band, and ZTF light curves in Z_g - and Z_r -band. These light curves allow us to constrain the temperature and distribution of spots on K2-25.

We derived the periodic signals in the light curves using the Generalized Lomb-Scargle Periodogram (GLS; Zechmeister & Kürster 2009) in the Python package *PyPeriod* (Czesla et al. 2019). We searched for the period of the light curves between 1 and 20 days and obtained the strong GLS power peak at ~ 1.88 days in all light curves (Figure 1). False alarm probability (FAP) values below 10^{-3} indicate robust detection for those periods. The one-day alias of that signal at ~ 2.14 days also shows a strong peak in the power, especially in ZTF light curves, because the ZTF data is collected every few nights.

The mean of the derived periods weighted by the errors was calculated to be 1.87708 ± 0.00066 day, and we adopted this value as the stellar rotation period P_{rot} . This value is consistent with the previously reported value $P_{\text{rot}} = 1.88 \pm 0.02$ day from the K2 light curve (Mann et al. 2016).

3.2 Monitoring light curve analyses - modulation amplitudes

We folded the light curves by the period $P_{\text{rot}} = 1.87708$ days, assuming that the brightness variability was stable during the observation window and there was no red noise (time-correlated noise) in the

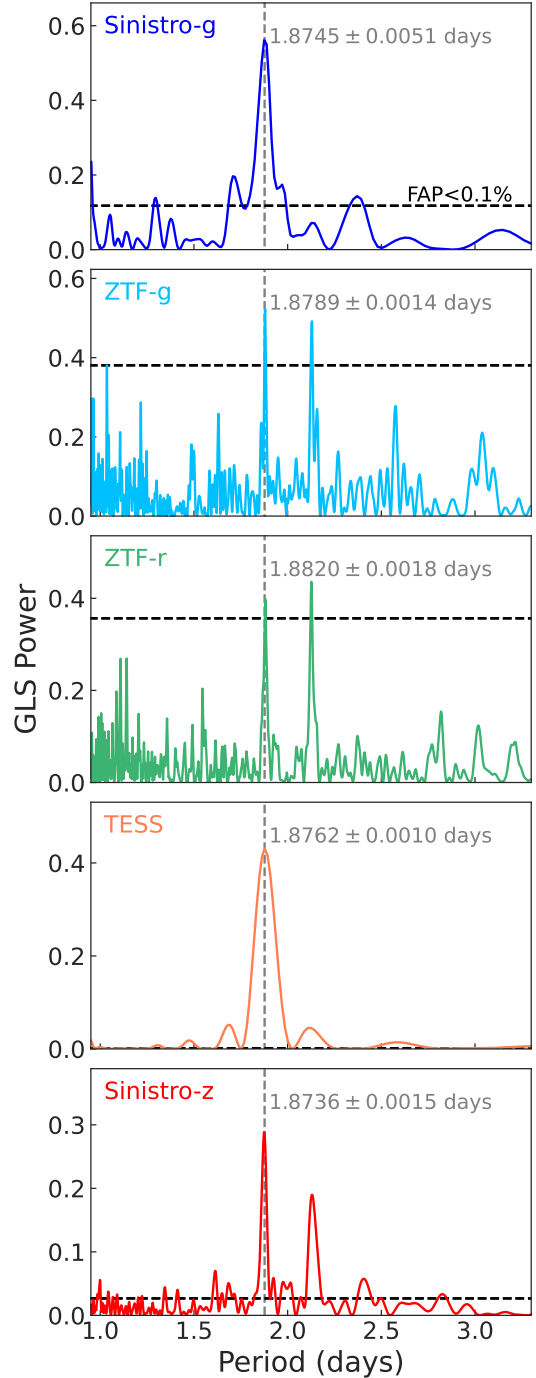


Figure 1. Results of period analysis for Sinistro-*g*, ZTF-*g*, ZTF-*r*, TESS, and Sinistro-*z* bands. The vertical lines for each panel show the detected period (1.88 days). The strong peak at ~ 2.14 days show the one-day alias of the signal. The horizontal lines indicate the false alarm probability at 0.1%. All light curves show clear periodicity.

light curves in all bands. It is possible that instrumental systematics behave as red noise in the light curves, but they are unlikely to be correlated with the stellar rotation phase. The data points were binned every 0.02 day in all bands in the following analyses.

We assumed that all the phase-folded light curves have local maxima and minima at the same phases and differ only in amplitude, and the light curves can be simply modeled as a summation of sine

Table 2. Summary of the observational data used in the analyses, where N_T indicates the number of transits counted from the reference transit-centre time T_0 .

Monitoring photometry				
Date	Instrument	Filters	Exposure Times (sec)	
2021 Oct 12 - Nov 06	TESS	TESS	120	
2021 Oct 02 - Nov 05	Sinistro	SDSS g	120	
2021 Oct 13 - 2022 Jan 31	Sinistro	Pan-STARRS z_s	40	
2021 Jul 05 - 2022 Mar 02	ZTF	Z_g, Z_r	30	
Transit photometry				
Date	Instrument	Filters	Exposure Times (sec)	N_T
2021 Dec 08	MuSCAT2	SDSS g, r, z_s	60, 45, 15	299
2021 Dec 22	MuSCAT2	SDSS g, r, z_s	60, 45, 15	303
2021 Dec 29	MuSCAT2	SDSS g, r, i, z_s	60, 45, 30, 15	305
2022 Jan 05	MuSCAT2	SDSS g, r, i, z_s	60, 45, 30, 15	307
2022 Jan 08	MuSCAT3	SDSS g, r, i, z_s	120, 50, 23, 15	308
2022 Jan 29	MuSCAT3	SDSS g, r, i, z_s	150, 45, 23, 15	314

	a_i	b_i	c_i
$i = 1$	0.00892	0.5521	0.9893
$i = 2$	0.00228	0.6567	1.9693

Table 3. Optimum values for a_i , b_i , and c_i in Equation 1 to fit the phase-folded TESS light curve.

functions. The derivation of the amplitudes had two steps. First, we optimized the TESS light curve by a summation of the sine functions as the reference model. We used the TESS light curve here as it has the most clear modulational shape. Second, we modelled the other light curves by changing the amplitude and offset of the reference model.

In the first step, the assumed reference model $f_{\text{TESS}}(\mathbf{p})$ along with the stellar rotational phase \mathbf{p} is described as

$$f_{\text{TESS}}(\mathbf{p}) = \sum_{i=1}^{N_s} \{a_i \sin 2\pi(b_i \mathbf{p} - c_i)\}, \quad (1)$$

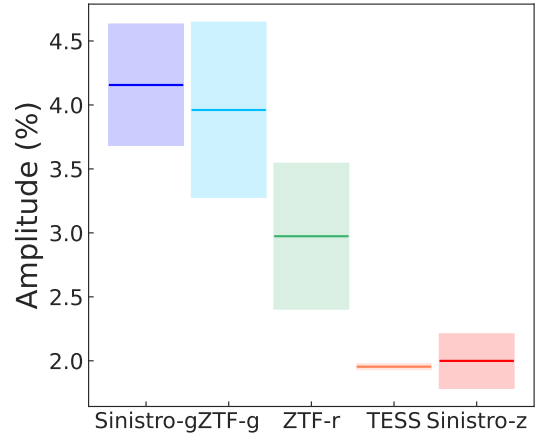
where a_i , b_i , and c_i are the parameters to be optimized. The optimization was performed using `scipy.optimize`, to make the chi-squared value smallest for the TESS light curve. The optimum parameter values are summarized in Table 3. The number of sine-curves N_s was selected to be 2 because the Bayesian information criterion (BIC) became smallest when the N_s value was tested from 1 to 4.

In step two, the flux f_B at each band $B = \{\text{Sinistro-g}, \text{ZTF-g}, \text{ZTF-r}, \text{and Sinistro-z}\}$ is represented by the $f_{\text{TESS}}(\mathbf{p})$ with the optimum parameters in Table 3, as in the following equation,

$$f_B(\mathbf{p}) = A_B \times \frac{f_{\text{TESS}}(\mathbf{p})}{A_{\text{TESS}}} + (\text{const.})_B \quad (2)$$

where A_B is the amplitude and $(\text{const.})_B$ is the offset at each band. For each band independently, we derived the value that maximises the log-likelihood with two parameters, A_B and $(\text{const.})_B$. Python package `emcee` was used for the parameter estimation via the Markov chain Monte Carlo method (MCMC). In this process, we found that the white noise in the light curves are larger than the photometric errors, which may be due to instrumental systematics or observing conditions. In order to correctly account for this noise, we amplified the errors so that the reduced chi-squared value approached 1, and we re-fit the model to the data with amplified errors.

Figure 2 summarizes the resulting A_B values with their uncertainties, and Figure 3 shows the phase-folded light curves plotted with


Figure 2. Derived modulation amplitude for the five light curves by sine-curve method (Section 3.2). The bands are listed from left to right in order of effective wavelength, from shortest to longest. A clear trend is seen: the longer the wavelength, the smaller the modulation amplitude. The values are summarized in Table A.2.

the derived best-fit models with 1σ uncertainties. It is clearly seen that the amplitude becomes smaller to longer wavelengths. As the Sinistro-g and ZTF-g have almost identical wavelength ranges, the weighted-mean value is calculated and used in the following analyses. We also tried another method using a Gaussian process (GP) model, which is more flexible for modelling the light curves, to independently derive the modulation amplitudes (see Appendix A2) and confirmed that the results are consistent.

3.3 Derivation of spot temperature and covering fraction

The differences in the amplitude at each wavelength reflect differences in the spot contrast, defined as the spot intensity relative to the photosphere. Based on that, we derive the spot temperature and covering fraction from the modulation amplitudes in this section.

We note that spots visible regardless of the stellar rotation phase (referred to as “always-visible spots” hereafter) are not considered in this analysis. It has been noted that even with multi-band light curves, constraining the covering fraction of always-visible spots is challenging (Rosich et al. 2020). We also confirmed that the estimation of the spot temperature and spot covering fraction, which contributes to

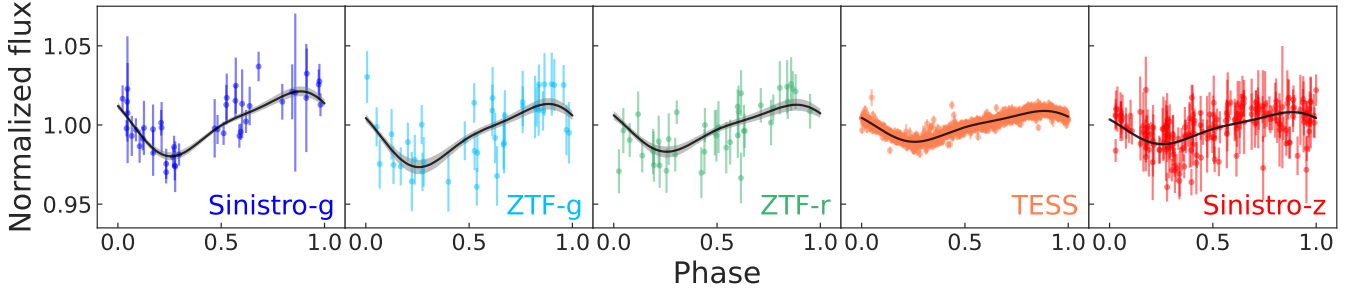


Figure 3. The phase-folded light curves and fitted model curves. The solid line shows the best-fit curves and the shaded region shows a 1σ deviation of model uncertainties, derived from the models drawn by the converged MCMC chains.

the brightness variation, remains unaffected whether the presence of always-visible spots is considered or not. On the other hand, while always-visible spots do not contribute to the brightness variation, they do cause TLSE during planetary transits. We account for them in the TLSE estimation in Section 3.5 by assuming various values of spot covering fraction.

Assuming that spots are scarcely visible during the peak brightness of a star and the spots with temperature T_{spot} and covering fraction f_{spot} during the dimmest phase, the amplitude of stellar brightness variation A_B at each band $B = \{g, r, \text{TESS}, z\}$ can be expressed by

$$A_B = |1 - c_B| f_{\text{spot}} \quad (3)$$

where c_B are the spot contrast (e.g., Equation 8 in Notsu et al. 2013). The spot contrast c_B is calculated from the following formula (e.g., Morris et al. 2018; Ikuta et al. 2023):

$$c_B = \frac{\int_B d\lambda \mathcal{T}_\lambda \mathcal{F}_{\lambda, \text{spot}}}{\int_B d\lambda \mathcal{T}_\lambda \mathcal{F}_{\lambda, \text{phot}}}, \quad (4)$$

where \mathcal{T}_λ is the filter transmission function and $\mathcal{F}_{\lambda, \text{spot/phot}}$ are the stellar flux from the spots or the photosphere at the temperature of T_{spot} and T_{phot} , respectively. We calculated c_B through Equation 4 using the filter profiles from the SVO Filter Profile Service (Rodrigo et al. 2012; Rodrigo & Solano 2020) and theoretical stellar spectra from the SVO Theoretical Model Services. For stellar spectra models, we used the BT-Settl model with the surface gravity $\log g = 5$ (in cgs), and the metallicity $[\text{Fe}/\text{H}] = 0$ dex. The spot temperature T_{spot} ranged from 2700 K to 3200 K in each 100 K step for the calculation and then interpolated. The photosphere temperature T_{phot} was fixed to be 3200 K, but we confirmed that the ~ 100 K difference of T_{phot} did not cause significant change to the relation of T_{spot} and c_B . Figure 4 shows the relation of calculated c_B and ΔT , which is defined by $T_{\text{phot}} - T_{\text{spot}}$, for all observed bands. The c_B values show band-dependent variation when ΔT is around 500 K, but the variation gets smaller when ΔT is close to 0 K or more than 1000 K, in the case of $T_{\text{phot}} = 3200$ K.

The combination of Equations 3 and 4 enables us to estimate the two unknown values, T_{spot} and f_{spot} from the estimated amplitude A_B in each band. As there are four bands in our analysis, T_{spot} and f_{spot} can be obtained simultaneously by formulating four of these equations with each error. The parameters are set to ΔT and f_{spot} , and the best parameter values were searched to describe the observed amplitudes for the four bands by calculating chi-squared values. We used MCMC package emcee for the parameter estimation. We put prior for ΔT to take positive values and f_{spot} to take values between 0 to 1.

Figure 5 shows the posterior distribution of the parameters using

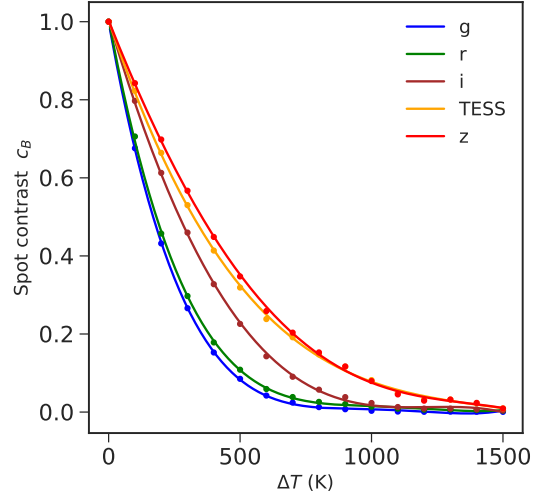


Figure 4. Relation of calculated spot contrast c_B to ΔT for each observed band $B = \{g, r, i, z, \text{TESS}\}$. ΔT represents the difference of spot temperature from the stellar surface temperature fixed at 3200 K. The wavelength dependence of the value of c_B is greatest around $\Delta T = 500$ K.

corner (Foreman-Mackey 2016). Although they are highly correlated, we derived the 2σ upper limit of ΔT is 190 K and f_{spot} is 61%. Note that we did not consider the possibility of spots with temperature higher than the stellar photosphere (referred to as “bright spots”). We discuss the case for bright spots in Appendix A4.

3.4 Investigation of the spot distribution

To evaluate the analysis of estimating spot temperature and covering fraction only from the amplitudes in multi-band light curves (Section 3.3), we further explored possible spot distributions using a spot mapping method (Ikuta et al. 2020, 2023). Given that there are known degeneracy in various spot distributions as a solution to the starspot mapping from the light curves (Basri & Shah 2020; Ikuta et al. 2020; Luger et al. 2021a), this study adopted the method of trying out several patterns of spot distribution and exploring their trends rather than searching for a single solution.

We used an analytical spotted model macula (Kipping 2012) as in Ikuta et al. (2023). It calculates the flux relative to the spotless photosphere assuming a particular stellar inclination angle, for a specified number of circular spots characterized by four parameters:

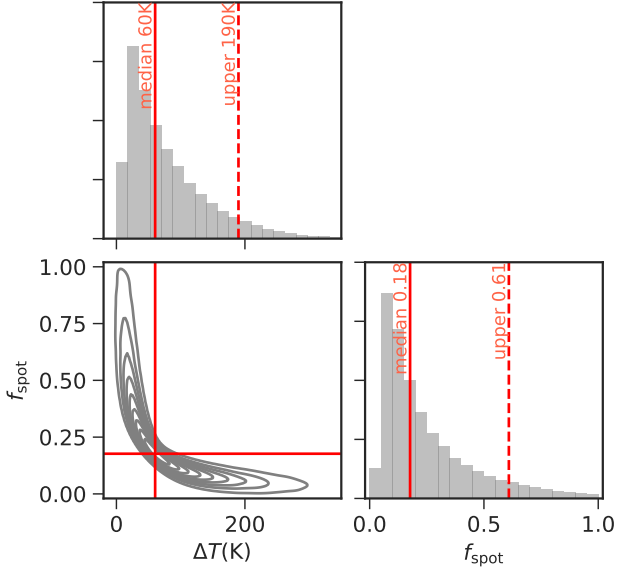


Figure 5. Posterior distribution of the spot temperature difference $\Delta T = T_{\text{phot}} - T_{\text{spot}}$ and the spot covering fraction f_{spot} . The red solid lines show the median values and the dashed lines show the upper limit with the 2σ level.

spot contrast, radius, latitude, and longitude (for more details, see Ikuta et al. 2023).

We calculated the light curves in g , r , TESS, and z -band under different spot contrast and stellar limb-darkening coefficients. The spot temperature was set to be identical for all spots. The spot contrast at each band was calculated by Equation 4 under the assumed temperature. The limb-darkening coefficients were calculated by the package PyLDTk (Parviainen & Aigrain 2015; Husser et al. 2013), assuming the stellar effective temperature $T_{\text{eff}} = 3207 \pm 58$ K, metallicity $[\text{Fe}/\text{H}] = 0.15 \pm 0.03$ dex, and stellar surface gravity $\log g = 4.944 \pm 0.031$ (in cgs). The stellar inclination and the degree of differential rotation were set to 90 deg (Stefansson et al. 2020) and 0. The rotation period was set to 1 because the light curves were phase-folded.

We reproduced various patterns of stellar surface models, with the number of spots set to two, three, four, and five. In each spot configuration with the number of spots of N_s , the light curve model was generated with $3N_s + 1$ parameters: radius, latitude, and longitude for each spot and ΔT . Since a larger number of parameters require a higher computational cost to obtain the optimal values, we provided some additional settings to simplify the calculations. First, we fixed the T_{phot} at 3200 K. Also, the latitude of any spot was restricted to taking only positive values. It is because the stellar inclination of K2-25 is ~ 90 deg so it is impossible to determine whether a spot is on the northern or southern hemisphere of the star. For spot size, we set uniform prior so that the maximum spot radius was 30° . We limited ΔT to be a positive value so that faculae (or any bright spots) were not considered.

At each number of spots N_s , we derived the posterior distributions using emcee to fit the reproduced light curves with the observed ones by calculating the chi-squared values. In the calculation, we adopted the amplified uncertainties of the observed light curves calculated in Section 3.2.

In addition, to compare the results by spot mapping with those from the amplitude, we calculated the spot covering fraction f_{spot} from the posterior distribution, by the summation of the projected

area of each spot (Equation 11 in Ikuta et al. 2020) at the minimum of the light curve.

Figure 6 shows the posterior distributions of ΔT and f_{spot} at each spot number case using corner (Foreman-Mackey 2016). The 2σ upper limit of ΔT was 142, 86, 78, 70 K and the upper limit of f_{spot} was 18, 31, 35, 41% for two, three, four and five spots cases, respectively.

While the two-spot case showed slightly different values, the upper limit values were similar for more than three spots. The model evidence was calculated via the importance sampling algorithm (e.g., Díaz et al. 2014) as well as Ikuta et al. (2020). The logarithm of the model evidence was calculated to be -711.34 , -707.81 , -706.60 , and -705.78 for two, three, four, and five-spot models, respectively. The model evidence is almost equal for the three, four, and five-spot cases within a factor of 8 ($\sim \exp(2.02)$), while the two-spot case showed relatively lower model evidence by three orders of magnitude ($\sim \exp(5.56)$) than the five-spot case. Then, the model with more than three spots is preferred in the model comparison (Kass & Raftery 1995). The joint posterior for the three-spot case is shown in Figure A.11 using corner (Foreman-Mackey 2016).

Figure 7 visualises the best-fit spot distribution at phase = 0 in the Mollweide projection for the two, three, four and five-spot cases. In the case of two spots, spots appear in the higher latitude (> 60 deg for both spots in the best-fit values) whereas in the case of three or more spots, they are found to be distributed similarly at about similar latitudes around 38 deg, while each spot latitude value has large (> 15 deg) uncertainties. In any case, the optimal solution preferred a pattern where the spot is barely visible when the star is brightest.

We note that our calculation does not take spot overlaps into account (i.e. the overlapping spots are calculated to be twice as dark). The spot latitude is restricted to take only positive values (northern hemisphere) because of the degeneracy with negative values (southern hemisphere) under the stellar inclination of ~ 90 deg. This overlap could be eliminated if one of the overlapped spots is placed alternately on the southern hemispheres.

The resulting upper limit of spot temperature and spot covering fraction (Figure 6) by spot mapping was consistent with the result of amplitude-spot temperature relations (Figure 5). We will further discuss the results in Section 4.1.

3.5 Estimation of transit light source effect

From the derived spot characteristics, we estimated how much the observed transit depths were affected by spots. The degree of TLSE to the transit depth at each wavelength is quantified by the contamination factor ϵ_λ (Rackham et al. 2017) as follows:

$$\delta_{\lambda,\text{obs}} = \epsilon_\lambda \delta_{\lambda,\text{true}}, \quad (5)$$

where $\delta_{\lambda,\text{obs}}$ is the observed transit depth at each wavelength and $\delta_{\lambda,\text{true}}$ is the true transit depth originating from the planetary atmosphere. From Rackham et al. (2018), the ϵ_λ value is determined by the ratio of the flux from the photosphere to the flux from the transit chord. Simply, it is calculated by the equation

$$\epsilon_\lambda = \frac{\mathcal{F}_{\lambda,\text{phot}}}{f_{\text{spot}}\mathcal{F}_{\lambda,\text{spot}} + (1 - f_{\text{spot}})\mathcal{F}_{\lambda,\text{phot}}}. \quad (6)$$

For each band, the equation can be represented as

$$\epsilon_B = \frac{1}{1 - f_{\text{spot}}(1 - c_B)}. \quad (7)$$

using the spot covering fraction f_{spot} and spot contrast c_B at the band B , obtained from equations (3) and (4) (Section 3.3). Here, we

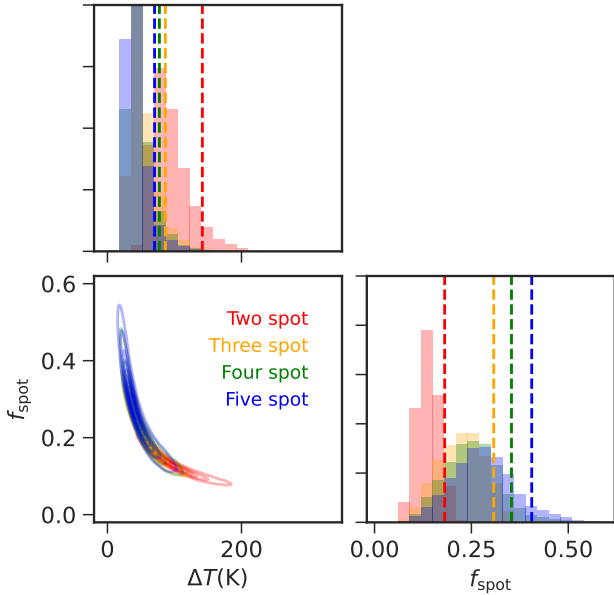


Figure 6. Posterior distribution of ΔT and f_{spot} , with two, three, four, and five-spot cases shown in red, orange, green and blue. The dashed lines indicate the 2σ upper limit of ΔT and f_{spot} at each case.

assume that there are no spots in the transit chord. This should be a reasonable assumption based on the fact that our observations show no signs of spot crossings (see Appendix A6).

Figure 8 shows the contamination factor (Equation 6) for each wavelength, assuming spots with a temperature of 3100 K on the stellar surface with a temperature of 3200 K as a reasonable assumption from our estimation of ΔT from the stellar brightness variability (Sections 3.3 and 3.4). As the f_{spot} can be larger if there are always-visible spots, we calculated the TLSE with different spot covering fractions from 5 % to 30 %. It is clearly seen that TLSE is larger in the optical wavelength range than in the infrared. In the near-infrared wavelength range that is important for the atmosphere characterization, the value of ϵ_λ varies by up to 1%; as the transit depth of K2-25 is $\sim 1\%$, this is expected to result in a transit depth variation of 100 ppm.

Separately, TLSE can also be calculated from the mapping results. Since Equation 6 represents the ratio of the flux coming from the spotless surface to the current stellar surface, we can divide the maximum value of the flux by the flux coming from the star at each rotation phase derived from the spot mapping. In this approach, the information regarding the spot positions and stellar limb darkening, which are known to potentially influence the estimation of TLSE (Thompson et al. 2024), was incorporated, as it directly utilizes the results of spot mapping. We confirmed that the typical TLSE value derived by this method was comparable to the value calculated by the method described above. This approach also enables the prediction of TLSE variations across different stellar rotational phases. Further details are given in the Appendix A5.

3.6 Transit light curve analyses

In this section, we focus on the transit light curves taken by the MuSCAT2, MuSCAT3, and TESS (summarized in Table 2). MuSCAT2 and MuSCAT3 observed the transits of K2-25 b six times in g , r , and z band, and four times in i band. TESS observed the six transits.

Therefore, we have 28 transit light curves in total (Figure 10). We analysed these transit light curves to derive the transit depths at each band to evaluate the degree of TLSE.

We jointly fit all 28 light curves using the mean models defined by the transit parameters and noise models defined as Gaussian processes (GP). The parameters, priors, and derived values from the following procedures are summarized in Table 4.

For the mean model of the planetary transit, we used the package *batman* (Kreidberg 2015), which is based on the analytic formula in Mandel & Agol (2002). As transit parameters, we adopt the transit-centre time T_0 , the orbital period P_{orb} , the orbital semi-major axis over the stellar radius a/R_\star , the impact parameter b , and the ratio of the planetary radius to the stellar radius R_p/R_\star . Only R_p/R_\star values were set as different parameters for each band. We assumed a linear ephemeris, as we did not detect any transit timing variations from our light curves. As the previous studies have shown K2-25 b should have an eccentric orbit (Thao et al. 2020; Stefansson et al. 2020), we added two more parameters $\sqrt{e} \cos \omega$ and $\sqrt{e} \sin \omega$, where e and ω are the eccentricity and longitude of periastron, respectively. In addition, modified quadratic limb-darkening coefficients (q_1, q_2) were set as parameters for each band (Kipping 2013). We used normal priors (Gaussian priors) for T_0, P, b based on the values in Stefansson et al. (2020), and normal priors for the limb-darkening coefficients based on the theoretical calculation by the package *PyLDTK* assuming the stellar effective temperature $T_{\text{eff}} = 3207 \pm 58$ K, metallicity $[\text{Fe}/\text{H}] = 0.15 \pm 0.03$ dex, and stellar surface gravity $\log g = 4.944 \pm 0.031$ (in cgs). In addition, we set the normal prior for stellar density ρ_\star to the value derived from Stefansson et al. (2020). Uniform priors were set for the other parameters.

To account for baseline trends in light curves, we used the GP with an approximated Matérn-3/2 kernel:

$$k_{MA}(\tau) = \frac{1}{2} \sigma^2 \left[(1 + 1/\varepsilon) e^{-(1-\varepsilon)\sqrt{3}\tau/\rho} + (1 - 1/\varepsilon) e^{-(1+\varepsilon)\sqrt{3}\tau/\rho} \right] \quad (8)$$

which is implemented in *celerite* (Foreman-Mackey et al. 2017; Foreman-Mackey 2018). Here, τ is the absolute time difference of each observing point, meaning that a data point is correlated with another data point. The hyperparameters σ and ρ determine the correlation of the data points: σ corresponds to the amplitude of correlation strength, and ρ is the timescale of the exponential decay. ε was fixed to 0.01 by default. Assuming that the baseline variation is caused by the brightness variation of the star itself or the wavelength-dependent instrument noise, we set hyperparameters for each band. As we do not know any prior information on these hyperparameter values, we set log-uniform priors for the hyperparameters.

As shown in Figures 10 and 11, we jointly optimized 28 transit light curves in total with the mean and noise models. The total number of parameters and hyperparameters were summed up to 31. The parameter estimation was performed using *emcee*, and the derived values are listed in Table 4. The derived transit depths for each band are also shown in Figure 13. Considering the large uncertainties in g and TESS-band, we do not see significant transit depth dependence on the colour.

3.7 Constraints on spot temperature and covering fraction from transit depths

As shown in Figure 8, the TLSE by dark spots makes the observed transit depths larger in shorter-wavelength bands in the optical. The derived transit depths did not show such a trend, although their uncertainties are large. Independently of the method obtained from the

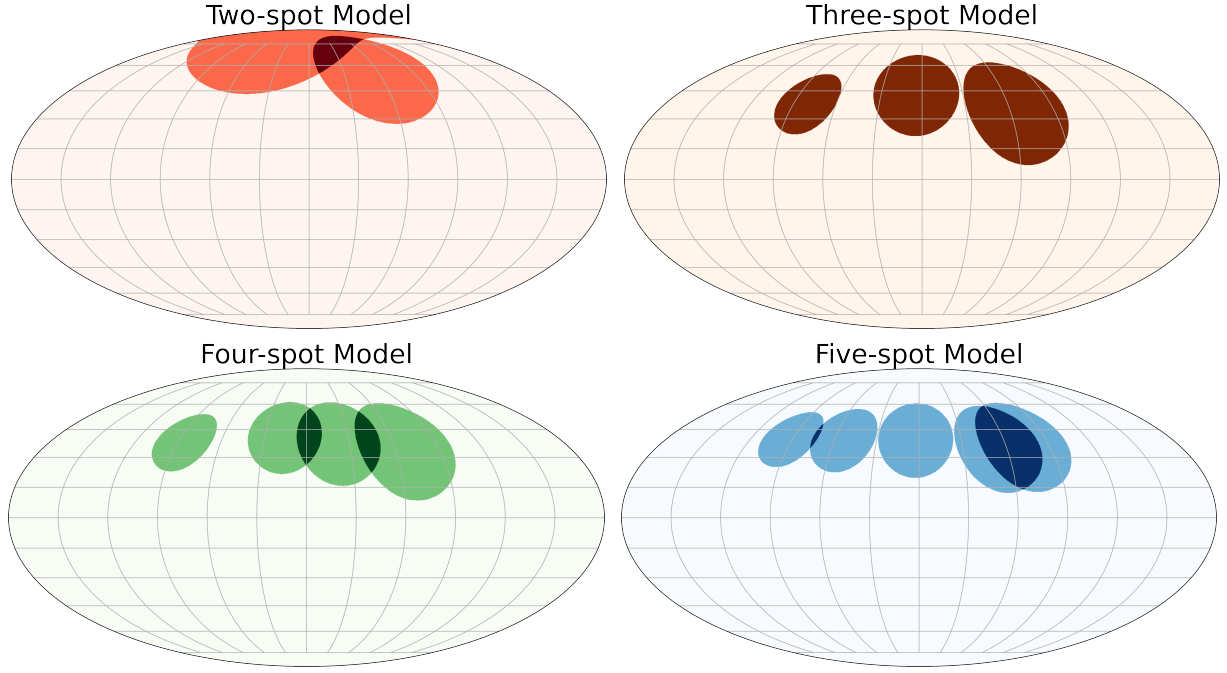


Figure 7. Spot map with optimum spot parameters for the two, three, four, and five-spot cases shown in red, orange, green and blue, respectively. The spots are located at high altitudes in the two-spot case. In cases with a larger number of spots, the spots show a similar distribution in the mid-latitude zone.

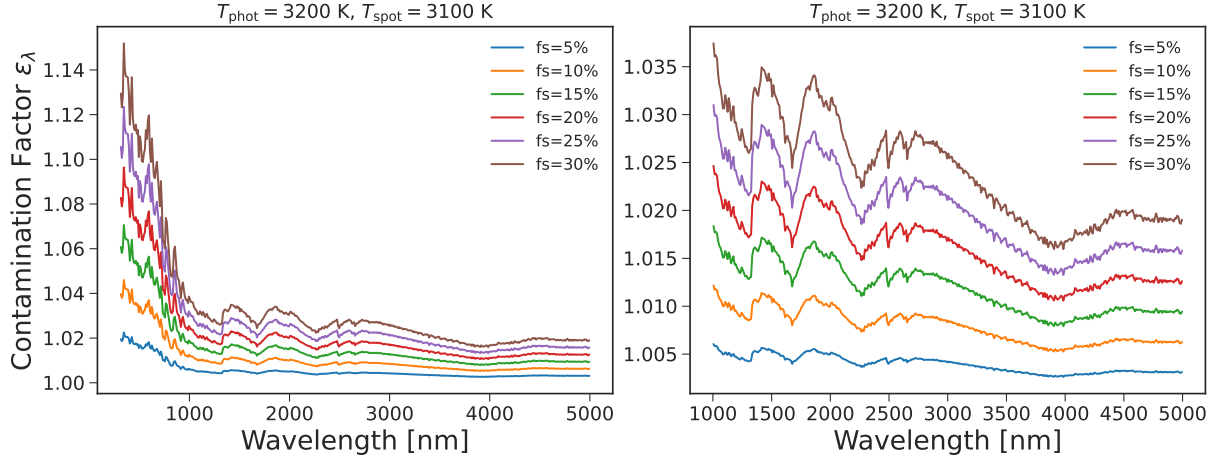


Figure 8. Calculated TLSE for each possible spot covering fraction f_{spot} , assuming the spots with $T_{\text{spot}} = 3100$ K on the photosphere temperature $T_{\text{phot}} = 3200$ K. The right figure is just a close-in to the wavelength over 1000nm. TLSE works strongly in the optical, and it fluctuates the transit depth by about 1% in the near-infrared.

monitoring light curves, we investigated the possible spot characteristics only from the transit depths observed by MuSCAT2/3 and TESS.

Assuming the true transit depth is constant for all observed bands (i.e., flat transmission spectra model), The observed transit depths at each band δ_B can be described as

$$\delta_B = \epsilon_B \delta_{\text{true}}, \quad (9)$$

where ϵ_B is a contamination factor for each band and δ_{true} is a true transit depth (constant value). ϵ_B for each band is calculated through the Equation 7. We modelled the δ_B for band $B = \{g, r, i, z, \text{TESS}\}$ with three parameters, ΔT , f_{spot} , and δ_{true} . We set uniform prior $\mathcal{U}(0, 1500)$ for ΔT and $\mathcal{U}(0, 1)$ for f_{spot} . δ_{true} was restricted to

take only positive values. The parameter estimation was done using emcee.

Figure 9 shows the derived posterior distribution using corner (Foreman-Mackey 2016). The 2σ upper limit of ΔT and f_{spot} values were 1427 K and 0.56, respectively. This means that little restriction could be placed on the spot characteristics from only the wavelength dependence of the transit depths. The posterior of ΔT shows a weak bimodal distribution, which is attributed to the fact that the obtained transit depths are consistent with flat considering the uncertainties and does not show a strong wavelength dependence. This is because the wavelength dependence of the spot contrast values is small at both low and high ΔT values, as shown in Figure 4. However, for large values of ΔT , either very small f_{spot} values or δ_{true} values will

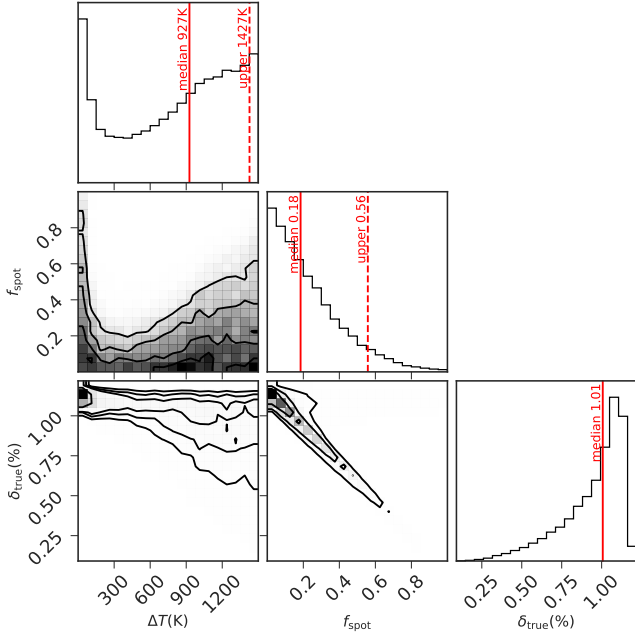


Figure 9. Posterior distribution of the spot temperature difference ΔT , the spot covering fraction f_{spot} , and the constant transit depth to explain the observed transit depths.

be required, which is unlikely in light of the other observed facts. Nevertheless, models with low-temperature spots spread over a wide area were ruled out. These results were consistent with the results from the monitoring light curves (Figure 5, 6).

We also tried to derive ΔT , f_{spot} , and δ_{true} by jointly fitting the transit depths and modulation amplitudes (Section 3.3). The derived posterior distribution of the parameters was almost identical to the results from the fitting of modulation amplitudes (Figure 5), meaning that the spot characteristics are constrained much better from the multi-band modulation amplitudes than the transit depths, considering the quality of our datasets.

4 DISCUSSION

4.1 Characteristics of spots on K2-25

From the amplitudes of stellar brightness variations (Sections 3.2 and 3.3), we derived the spot temperature T_{spot} to be $\Delta T < 190$ K lower than the assumed photosphere temperature of $T_{\text{phot}} = 3200$ K, and the spot covering fraction f_{spot} to be $< 61\%$ with 2σ confidence level (Figure 5). While the upper limit of spot covering fraction $f_{\text{spot}} < 61\%$ is not a strong constraint, the upper limit of spot temperature, $\Delta T_{\text{spot}} < 190$ K, provides sufficient information to scrutinize spot properties and assess the extent of the TLSE, as detailed in Section 4.4.

Furthermore, we explored the potential spot distribution through spot mapping (Section 3.4). Despite limiting the number of spots up to five due to parameter degeneracies, we determined that cases involving three or more spots exhibited a general trend in spot distribution. A further increase in the number of spots could elevate the value of f_{spot} due to certain spots not contributing to brightness variations (i.e., always visible spots). Nonetheless, ΔT remained rel-

atively stable as the number of spots increased, indicating minimal variation in ΔT prediction with different numbers of spots.

Comparing the results from the amplitude (Figure 5) and spot mapping (Figure 6), the spot mapping results showed more strict constraints on both the spot temperature and spot covering fraction in each spot number case. This is because the spot mapping takes into account not only the amplitude of the brightness variation but also the shape of the light curves. Possible sizes and positions of the spots were determined in order to represent the smooth brightness variations of K2-25 monitoring light curves, which resulted in a stronger constraint on the spot temperatures. We note that spot mapping entails various assumptions (e.g., assuming a perfectly circular spot, a small number of spots, etc.). The results may vary if a more flexible spot configuration is allowed (e.g., Luger et al. 2021b). Therefore, the more conservative results obtained from the amplitudes are used in the discussion part of this paper.

In addition, from the wavelength dependence of the transit depths (Section 3.7), we also derived the 2σ upper limit of both spot temperature difference (< 1184 K) and covering fraction (< 0.43) (Figure 9). Despite weak constraints due to transit depth uncertainties, we can rule out the extreme cases with large spot temperature differences and large spot covering fractions. The results are consistent with the results derived by stellar brightness monitoring. Consequently, the resulting spot characteristics were in agreement with the overall features from the modulation amplitudes (Section 3.3), spot mapping (Section 3.4) and from transit depths (Section 3.7).

4.2 Effectiveness of simultaneous multi-band observations

In our study, simultaneous multi-band monitoring observations allowed us to achieve exceptional precision to constrain the spot characteristics, especially spot temperature difference ΔT . This is mainly because, thanks to the multi-band light curves, degeneracies between spot latitude, spot size and spot temperature are broken to some extent. When the spot is located near the poles, the wavelength dependence of the dimming due to the spot is smaller because of limb-darkening. In this study, the wavelength dependence of the brightness variability amplitudes resulted in taking a low likelihood value of the case with spots near the pole, thereby better defining the spot size and temperature.

We confirmed that our method using multi-band light curves from TESS and ground-based telescopes resulted in better constraint especially on spot temperature estimation, comparing the spot mapping result using five light curves and using only the TESS light curve (details are in Appendix A8). The result of spot mapping effectively depends on the TESS light curve with higher time cadence and photometric precision, but multi-band data from ground-based telescopes are useful in putting further constraints on the solutions.

There are a few studies of such multi-band (but not simultaneous) monitoring observations conducted for M-dwarfs. Morris et al. (2018) analysed the monitoring light curves of an M8 star TRAPPIST-1, by Kepler and Spitzer, and constrained the spot temperature to be extremely hot ($T_{\text{spot}} \gtrsim 5300 \pm 200$ K). Miyakawa et al. (2021) analysed the monitoring light curves of four M dwarfs in the Hyades cluster in the Kepler-band and J, H, K -band, and derived their spot temperatures within 1σ uncertainties of $\lesssim 700$ K.

Our observations constrained the T_{spot} values more precisely than these studies. This is because our observations obtained multi-band light curves in optical, which are more sensitive to spot temperature than in infrared. Also, simultaneity was important, as the spot characteristics may change in a timescale of the spot emergence and decay (Appendix A5).

Table 4. Priors and derived parameters of the transit analyses. $\mathcal{U}(A, B)$ indicates the uniform prior from A to B and $\mathcal{N}(X, Y^2)$ indicates the normal prior with the mean value X and standard deviation Y.

Parameter	Prior	Derived Value
<i>Primary transit parameters^a</i>		
T_0 [BJD]	$\mathcal{N}(2458515.64206, 0.00010^2)$	$2458515.642139 \pm 0.000095$
P [days]	$\mathcal{N}(3.48456498, 0.00000060^2)$	3.4845650 ± 0.0000005
$\sqrt{e} \cos \omega$	$\mathcal{U}(-1, 1)$	$-0.82^{+0.11}_{-0.04}$
$\sqrt{e} \sin \omega$	$\mathcal{U}(0, 1)$	$0.12^{+0.13}_{-0.09}$
a/R_\star	$\mathcal{U}(0, 100)$	20.8 ± 0.8
b	$\mathcal{N}(0.628, 0.04^2)$	0.65 ± 0.02
R_p/R_\star (g)	$\mathcal{U}(0, 1)$	$0.090^{+0.009}_{-0.010}$
R_p/R_\star (r)	$\mathcal{U}(0, 1)$	0.104 ± 0.004
R_p/R_\star (i)	$\mathcal{U}(0, 1)$	0.108 ± 0.002
R_p/R_\star (z)	$\mathcal{U}(0, 1)$	0.108 ± 0.002
R_p/R_\star (TESS)	$\mathcal{U}(0, 1)$	0.101 ± 0.005
<i>Derived parameters and additional constraint</i>		
e	-	$0.69^{+0.05}_{-0.10}$
ω [deg]	-	172^{+6}_{-14}
ρ_\star [g/cm ³]	$\mathcal{N}(14.7, 1.5^2)$	14.1 ± 1.5
<i>Limb darkening parameters^b</i>		
q_1 (g)	$\mathcal{N}(0.729, 0.011^2)$	0.721 ± 0.012
q_2 (g)	$\mathcal{N}(0.340, 0.002^2)$	0.343 ± 0.003
q_1 (r)	$\mathcal{N}(0.633, 0.012^2)$	0.631 ± 0.013
q_2 (r)	$\mathcal{N}(0.366, 0.003^2)$	0.367 ± 0.003
q_1 (i)	$\mathcal{N}(0.430, 0.008^2)$	0.421 ± 0.008
q_2 (i)	$\mathcal{N}(0.294, 0.003^2)$	0.298 ± 0.003
q_1 (z)	$\mathcal{N}(0.337, 0.007^2)$	0.322 ± 0.007
q_2 (z)	$\mathcal{N}(0.253, 0.003^2)$	0.262 ± 0.003
q_1 (TESS)	$\mathcal{N}(0.299, 0.004^2)$	0.299 ± 0.004
q_2 (TESS)	$\mathcal{N}(0.295, 0.002^2)$	0.295 ± 0.002
<i>Gaussian process hyperparameters</i>		
$\log \sigma$ (g)	$\mathcal{U}(-10, 5)$	-3.8 ± 0.3
$\log \rho$ (g)	$\mathcal{U}(-10, 10)$	-2.9 ± 0.3
$\log \sigma$ (r)	$\mathcal{U}(-10, 5)$	-4.2 ± 0.3
$\log \rho$ (r)	$\mathcal{U}(-10, 10)$	-2.8 ± 0.3
$\log \sigma$ (i)	$\mathcal{U}(-10, 5)$	-5.5 ± 0.4
$\log \rho$ (i)	$\mathcal{U}(-10, 10)$	-2.4 ± 0.4
$\log \sigma$ (z)	$\mathcal{U}(-10, 5)$	-6.6 ± 0.1
$\log \rho$ (z)	$\mathcal{U}(-10, 10)$	-4.2 ± 0.3
$\log \sigma$ (TESS)	$\mathcal{U}(-10, 5)$	-6.3 ± 0.2
$\log \rho$ (TESS)	$\mathcal{U}(-10, 10)$	-3.4 ± 0.5

^a For parameters with normal prior distributions, the mean and variance are adopted from [Stefansson et al. \(2020\)](#)

^b from $[u_1, u_2]$ values calculated by PyLDTk.

Our observations showed that simultaneous multi-band monitoring using a combination of ground-based and space-based telescopes will be effective in determining the ‘‘current’’ spot characteristics of the host star, for example, in future planetary atmosphere research.

4.3 Indication to the spot-photosphere temperature relations

Figure 12 shows the relation of $\Delta T_{\text{spot}} = T_{\text{phot}} - T_{\text{spot}}$ and T_{phot} values from this work in comparison with the ones from recent literature for cool dwarfs derived by various methods ([Berdyugina 2005](#); [Frasca et al. 2009](#); [Miyakawa et al. 2021](#); [Almenara et al. 2022](#); [Waalkes et al. 2023](#)).

There were several studies to derive the empirical relations of ΔT and T_{phot} with polynomial functions ([Berdyugina 2005](#); [Maehara et al. 2017](#); [Herbst et al. 2021](#)). [Berdyugina \(2005\)](#) reports that ΔT increases as the value of T_{phot} increases for both the dwarfs and giants. [Herbst et al. \(2021\)](#) updates the empirical relations by incorporating the latest samples, mainly for stars with effective temperatures of

$T_{\text{eff}} > 4500$ K. After [Berdyugina \(2005\)](#), a few observations slightly increased the number of samples with $T_{\text{eff}} < 4000$ K ([Frasca et al. 2009](#); [Miyakawa et al. 2021](#); [Almenara et al. 2022](#); [Waalkes et al. 2023](#)). The results of those studies and our result suggest that the overall trend almost corresponds to the empirical relationship, but a trend towards smaller ΔT with lower photosphere temperature, except for a young pre-main sequence M dwarf AU Mic ([Waalkes et al. 2023](#)).

Whereas the number of samples is still limited, these results suggest that the relations might no longer be suitable for M-dwarfs, especially with $T_{\text{eff}} \lesssim 3500$ K. It is important to note that in the prediction of the TLSE for each planetary system, T_{spot} values are often assumed based on the empirical formula mentioned above (e.g., [Rackham et al. 2018](#)). In such cases, there is a possibility of overestimating ΔT values (i.e., underestimating T_{spot} values). It is possible to update the relationship for M-dwarfs by adding samples with high-precision measurements of ΔT as future issues. In addition, the accumulation of the measurements on the T_{spot} for low-temperature stars would be

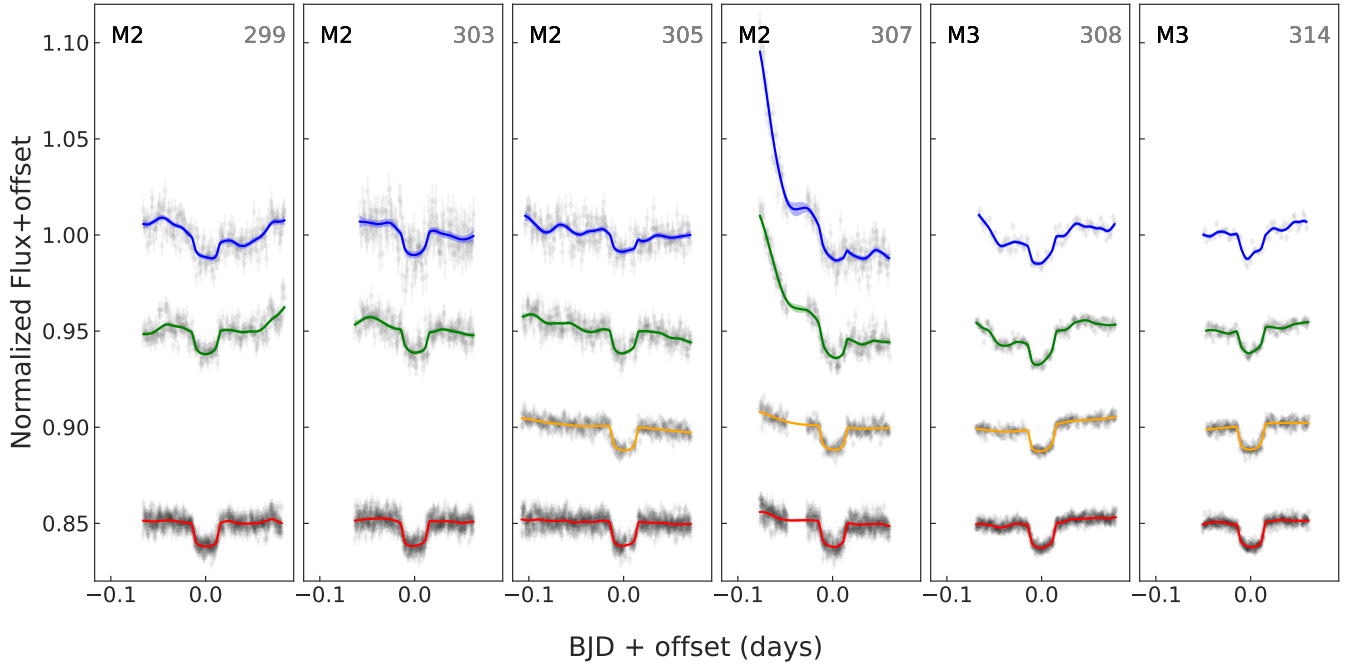


Figure 10. Transit light curves of K2-25 b taken with MuSCAT2 & 3 in g , r , i , z -band (from top to bottom) on each observing night. N_T number is shown next to each light curve. In each subplot, observed data points are shown in grey points, and best-fit transit + baseline models derived by GP regression are indicated in coloured lines. The shaded regions indicate the 1σ error of the GP model.

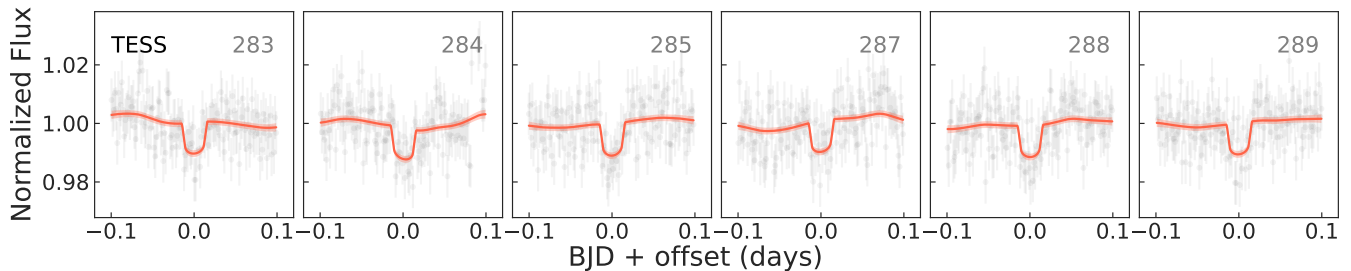


Figure 11. Similar to Figure 10 but for transit light curves taken with TESS. Note that TESS observations are not simultaneous with the MuSCAT2/3 observations.

useful in theoretical studies of the starspot properties. In Panja et al. (2020), the temperature dependence of the H^- opacity explains the trend of ΔT_{spot} and T_{phot} , and this reproduces the trend derived by Berdyugina (2005). However, the calculation has not yet been done for stars with temperatures lower than 3700 K (i.e., M0-type stars). It is important to increase observational data for the evaluation of these theoretical explanations.

4.4 Indication to the K2-25b atmosphere retrievals

In Figure 13, we show the derived transit depths of K2-25 b in five bands (g , r , i , z , and TESS-band) along the wavelength. We overplotted them with the previous transit depths derived by Thao et al. (2020), which used the data taken with Kepler, Sinistro i -band, MEarth, Spitzer channel 1, and Spitzer channel 2. We found that the transit depths from our observations have smaller overall values than the ones from Thao et al. (2020), despite the wavelength ranges being similar. However, given the large errors especially in the g , r ,

and TESS bands, all transit depths are consistent within a 2σ range. We did not ascertain the trend of deeper transit in the visible compared to the infrared, which was reported in Thao et al. (2020). This result might be due to some systematics from different observations, different analytical methods, and different stellar activity levels.

We also overlaid the calculated transmission spectrum models assuming TLSE and planetary atmosphere compositions. The atmosphere model with $100\times$ solar metallicity is calculated using the python package PLATON (Zhang et al. 2019) assuming the chemical equilibrium, from $R_\star = 0.2932R_\odot$ (Thao et al. 2020), $R_p/R_s = 0.108$ (this work), $M_p = 24.5M_\oplus$ and the equilibrium temperature $T_{\text{eq}} = 494$ K (Stefansson et al. 2020). The TLSE was calculated assuming the spots with $T_{\text{spot}} = 3100$ K and $f_{\text{spot}} = 15\%$, which are reasonable values from our monitoring observations.

While changing the y-axis offset as a parameter, we fit the models to data and calculated the chi-squared and reduced chi-squared values for four models: a flat atmosphere spectrum with and without TLSE, and a $100\times$ -Solar-metallicity atmosphere spectrum with and without

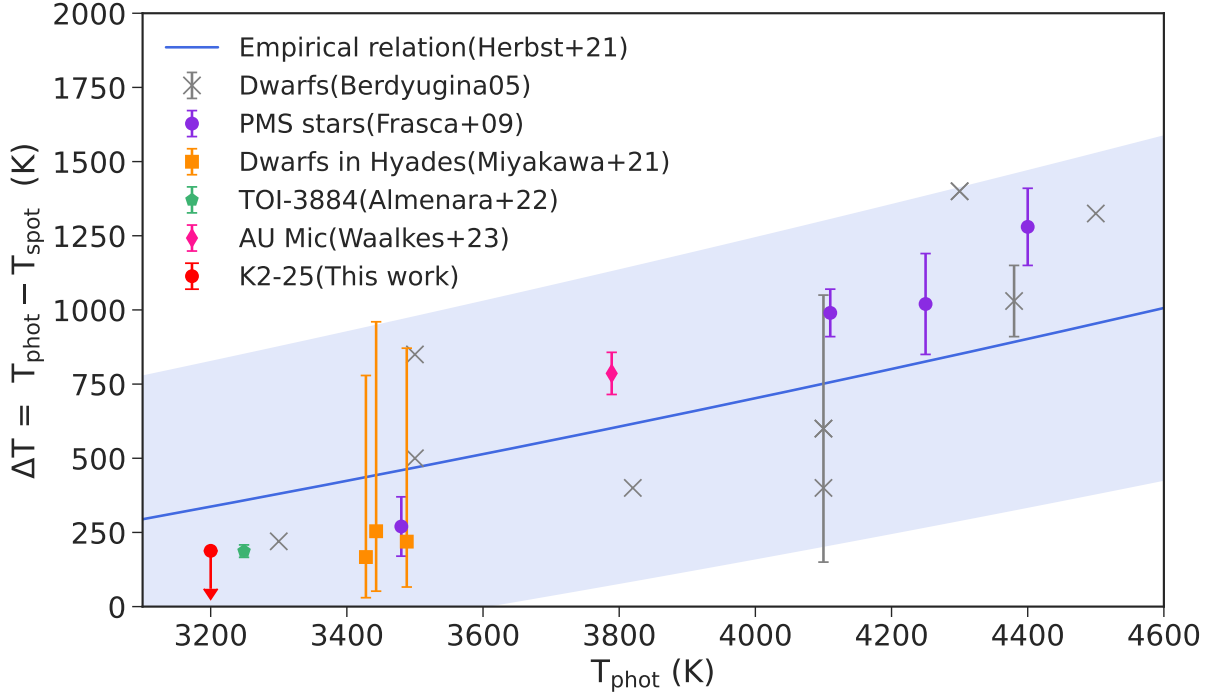


Figure 12. Relations between T_{phot} and temperature difference $\Delta T_{\text{spot}} = T_{\text{phot}} - T_{\text{spot}}$ for the dwarfs between 3000 K to 5000 K. The empirical relation and its uncertainties from Equation 4 in [Herbst et al. \(2021\)](#) (derived from dwarfs and giants in [Berdyugina \(2005\)](#)) are indicated in the blue line and filled regions. Note that data points without error bars are those for which the errors are not estimated. For the stars with $T_{\text{phot}} \lesssim 3500$ K, ΔT tend to show smaller values compared to the empirical relation.

TLSE. The values are listed in Table 5. We do not see a significant difference in chi-squared values for all models, in both cases using the transit depths only from this work and from this work combined with [Thao et al. \(2020\)](#).

While [Thao et al. \(2020\)](#) rejected the clear 100 \times solar metallicity model, our analysis shows that this possibility cannot be dismissed. This is not due to differences in stellar surface models, but mainly because the atmospheric model features were reduced due to the larger planetary mass estimates, with reference to the results of [Steffansson et al. \(2020\)](#). For the combined dataset from our work and [Thao et al. \(2020\)](#), the chi-squared value is slightly smaller when the spot effects are taken into account, for both the flat and 100 \times -Solar-metallicity atmosphere cases, but this is also not a statistically significant difference.

Also, in [Thao et al. \(2020\)](#), they pointed out that spot covering fractions of 22% to 36% are too large and unlikely given that the stellar variability is 0.5% to 2%, but our analysis does not rule out such a large spot covering fraction, considering the existence of spots that do not contribute to the stellar brightness variability.

It should be noted that the spectrum from [Thao et al. \(2020\)](#) is stacked, i.e. consisting of individual datasets taken between 2015 and 2017, while our spectrum was taken in 2021. Given that our observations show that the spot distribution in K2-25 varies on scales of hundreds of days (see Appendix A3), it would be not good practice to use all datasets to compare with models. We therefore stop here for a detailed comparison using both results. To make a real comparison for the atmosphere constraint of K2-25b, we need to simultaneously obtain spectra over a wide range of wavelengths with high-precision spectroscopy, such as by JWST.

As in Figure 8, the TLSE is not very significant in the JWST/NIRSPEC wavelength range (600 - 5000 nm) compared to

the optical. However, for example, when comparing the contamination factor at wavelength ~ 1500 nm and 4000 nm, there are some cases where the ϵ_{λ} differs by $\sim 1\%$. This means that even if the “true” transit depth is the same (i.e., flat transmission spectra), the observed depth differs by 100 ppm relative to each other.

Given the photometric precision of JWST’s observations, this effect cannot be ignored. We have confirmed from the simulation of JWST spectra using software PandExo ([Batalha et al. 2017](#)), that when K2-25 is observed with PRISM at JWST/NIRSPEC, a precision of < 100 ppm can be achieved in a single transit, although this depends on the wavelength binning. This indicates that stellar surface models need to be examined when inferring atmospheric models for K2-25 b from transmission spectroscopy by JWST. In that case, our knowledge of the spot temperature and the covering fraction of K2-25 from the monitoring observations is a good prior to investigating the stellar surface models. Of course, ideally, the monitoring observations should be conducted at the same time as the transmission spectroscopy by JWST.

4.5 Other stellar activity features on K2-25: indication for the future atmosphere research

We also investigated some other stellar activity signals on K2-25 from the analyses of multi-band light curves (see Appendix A3, A5 to A7 for details). We found there is a long-term variability of the modulation amplitude in a timescale of a few $\times 100$ days. This might be explained by the timescale of the change in the spot distribution. This means it is important to obtain the concurrent status of stellar activity when the transmission spectroscopy is conducted.

From the analysis of flare frequency, we confirmed three flares in K2-25 with the energy at $\sim 10^{33}$ erg, in a 21.76 days-long TESS

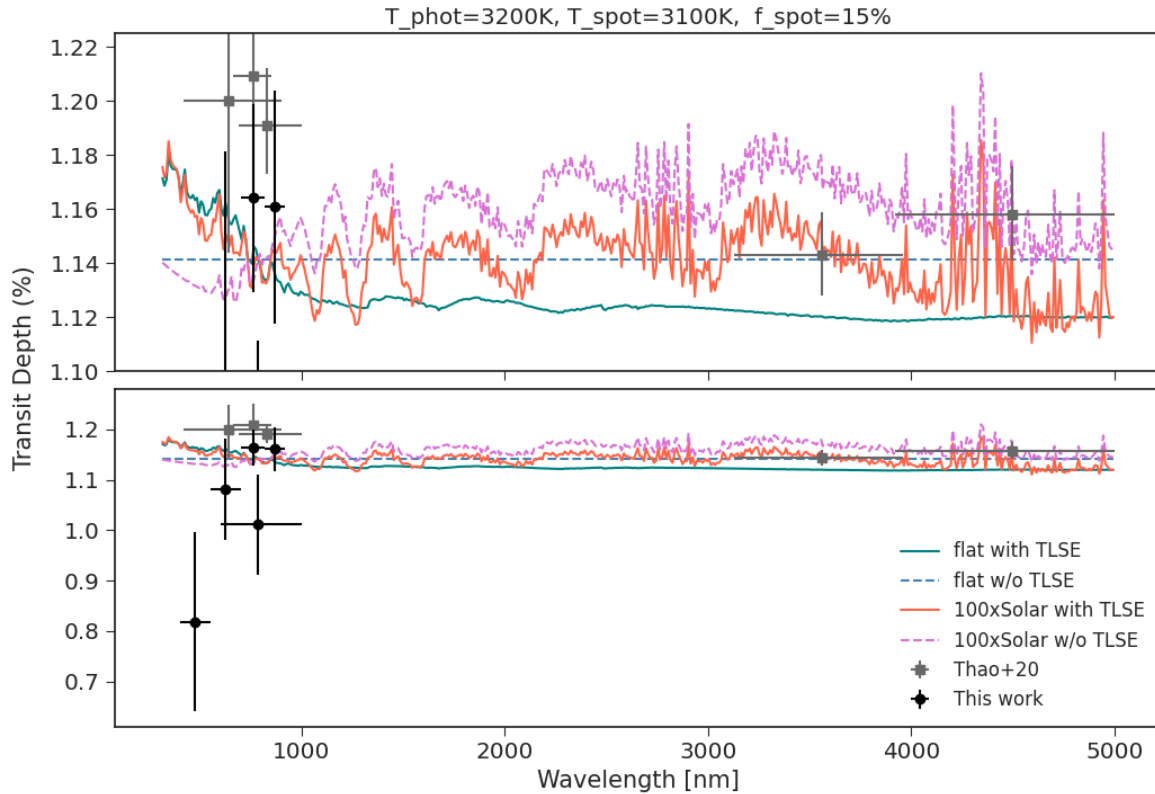


Figure 13. Generated transmission spectrum of K2-25b overplotted with the observed transit depths in multi-band. The black dots with errorbars indicate the transit depths by this work in *g*, *r*, *i*, TESS and *z*-band from left to right, and grey dots with errorbars indicate the values from [Thao et al. \(2020\)](#). The observed transit depths are compared with the planetary atmosphere models. Green/blue lines are the flat atmosphere model and orange/pink lines are the forward model generated by PLATON, with 100× solar metallicity atmosphere, with (solid) and without (dashed) the effect of spots (TLSE). The y-axis offset of each model was optimized for the data obtained in this work.

The top figure is the close-up version of the bottom figure.

Table 5. Calculated chi-squared values and reduced chi-squared values for each atmosphere model with and without spot effect, assuming $T_{\text{spot}} = 3100$ K and $f_{\text{spot}} = 15\%$. The values are calculated for (1) only using MuSCATs and TESS data from this work and (2) combined data from this work and from [Thao et al. \(2020\)](#) (T20).

Model	Data			
	(1)This Work		(2)This Work + T20	
	χ^2	reduced χ^2	χ^2	reduced χ^2
Flat with spot	6.82	1.70	10.6	1.17
Flat without spot	5.98	1.49	11.5	1.28
100×Solar with spot	6.50	1.62	13.1	1.46
100×Solar without spot	5.66	1.42	17.2	1.91

light curve. This is a typical flare frequency for a young mid-M star ([Günther et al. 2020](#); [Murray et al. 2022](#)), although the number of flare detections was limited because of the detection limit. Smaller flares should happen more frequently, which could be the dominant source of baseline fluctuation in transit light curves (especially in the blue-colour band). When performing high-precision transit observations using space telescopes, at least multiple observations should be made,

since flares may occur during the observation and cause the baseline modulation in the transit light curves.

5 CONCLUSION

In this study, we examined the stellar brightness variability of the young mid-M-dwarf K2-25 and analyzed the transits of its sub-Neptune companion K2-25 b using data from TESS and ground-based telescopes. Our aim was to investigate the characteristics of starspots within the system and their impact on transit observations.

The significance of our study stems from the utilization of (i,ii) “multi-band” and (iii) “simultaneous” observations, which enabled precise constraints on spot characteristics.

(i) Multi-band monitoring of stellar brightness provided robust constraints on spot temperature. Using monitoring light curves in four different bands (utilizing five different instruments/filters), we revealed the wavelength dependence of the amplitudes of stellar brightness modulation. From there, we found the spot temperature difference from the photosphere temperature of K2-25 to be < 190 K and the spot covering fraction to be $< 61\%$ with 2σ confidence level. These results were consistent with the one derived from spot

mapping, assuming two, three, four or five spot cases (Section 4.1). The derived spot temperature difference was smaller than the extrapolation of the empirical relation with the stellar photosphere temperature. This suggests that such an empirical relation is no longer suitable for M-dwarfs (Section 4.3).

(ii) Multi-band transit photometry was also obtained to constrain stellar surface models through the calculation of the TLSE. Although the derived transit depths by MuSCAT series and TESS had uncertainties too large to precisely constrain the spot temperature and covering fraction, we confirmed that the results were consistent with the spot characteristics constrained by the monitoring observations (Section 3.7). We calculated that the expected TLSE would distort the transmission spectrum of the system with the amplitude of ~ 100 ppm in the JWST/NIRSPEC wavelength range, which is detectable with JWST (Section 4.4).

(iii) This study was the first trial of taking stellar monitoring and transit observations simultaneously (Section 4.2). From the long-baseline light curves, we found that the spot distributions should change on timescales of hundreds of days. For more precise transit observations, it is important to know the spot distribution at each observing epoch.

There is room for further improvements to our methods, such as improving observation precision and refining stellar surface models for more precise derivation of stellar parameters from light curves. For example, faculae were not considered in our analysis because of the difficulty in quantifying their contributions to the light curves: faculae are known to become brighter towards the star limb (Norris et al. 2023). Although faculae are expected to contribute less to the brightness variability than spots because faculae are more widely distributed on the stellar surface (Johnson et al. 2021), how to handle the contribution from faculae to the light curve is a future issue.

Nevertheless, our investigation of the spot characteristics of an M-dwarf, using the best current instruments and methods, is an important step forward. Employing this method, along with further improvements as mentioned above, may be crucial for more accurate observations of planetary atmospheres with space telescopes, and for further studies of the stellar activity of M-dwarfs.

6 DATA AVAILABILITY

The TESS data can be accessed through the MAST (Mikulski Archive for Space Telescopes) portal at <https://mast.stsci.edu/portal/Mashup/Clients/Mast/Portal.html>. The ZTF data can be accessed through <https://irsa.ipac.caltech.edu/Missions/ztf.html>. The data taken by Sinistro, MuSCAT2 and 3 are available upon request to the authors. The SVO Filter Profile Service and theoretical stellar spectra can be obtained from the SVO Theoretical Model Services <http://svo2.cab.inta-csic.es/theory/main/>.

This work has utilized these public software: LCOGT BANZAI pipeline (McCully et al. 2018), PyPeriod (Czesla et al. 2019), corner (Foreman-Mackey 2016), celerite (Foreman-Mackey et al. 2017; Foreman-Mackey 2018), batman (Kreidberg 2015), PyLDTk (Parviainen & Aigrain 2015; Husser et al. 2013), emcee (Foreman-Mackey et al. 2013), PLATON (Zhang et al. 2019), PandExo (Batalha et al. 2017), Lllamaradas-Estelares (Mendoza et al. 2022), and Astropy (Astropy Collaboration et al. 2013, 2018).

7 ACKNOWLEDGEMENTS

We acknowledge Dr. Teruyuki Hirano and Dr. Kohei Miyakawa for their helpful insights and advice during the discussion process.

We acknowledge the use of public TESS data from pipelines at the TESS Science Office and at the TESS Science Processing Operations Center. Funding for the TESS mission is provided by NASA's Science Mission Directorate. This research has made use of the Exoplanet Follow-up Observation Program website, which is operated by the California Institute of Technology, under contract with the National Aeronautics and Space Administration under the Exoplanet Exploration Program. Resources supporting this work were provided by the NASA High-End Computing (HEC) Program through the NASA Advanced Supercomputing (NAS) Division at Ames Research Center for the production of the SPOC data products.

This work is partly based on observations made with the MuSCAT2 instrument, developed by ABC, at Telescopio Carlos Sánchez operated on the island of Tenerife by the IAC in the Spanish Observatorio del Teide.

This work makes use of observations from the Las Cumbres Observatory global telescope network. Some data in the paper are based on observations made with the MuSCAT3 instrument, developed by Astrobiology Center and under financial support by JSPS KAKENHI (JP18H05439) and JST PRESTO (JPMJPR1775), at Faulkes Telescope North on Maui, HI, operated by the Las Cumbres Observatory.

Based on observations obtained with the Samuel Oschin Telescope 48-inch and the 60-inch Telescope at the Palomar Observatory as part of the Zwicky Transient Facility project. ZTF is supported by the National Science Foundation under Grant No. AST-2034437 and a collaboration including Caltech, IPAC, the Weizmann Institute for Science, the Oskar Klein Center at Stockholm University, the University of Maryland, Deutsches Elektronen-Synchrotron and Humboldt University, the TANGO Consortium of Taiwan, the University of Wisconsin at Milwaukee, Trinity College Dublin, Lawrence Livermore National Laboratories, and IN2P3, France. Operations are conducted by COO, IPAC, and UW.

This work is supported by Grant-in-Aid for JSPS Fellows, Grant Number JP20J21872, JSPS KAKENHI Grant Numbers JP18H05439, 18H05442, 21K13955, 21K20376, and JST CREST Grant Number JPMJCR1761.

We acknowledge financial support from the Agencia Estatal de Investigación of the Ministerio de Ciencia e Innovación MCIN/AEI/10.13039/501100011033 and the ERDF "A way of making Europe" through project PID2021-125627OB-C32, and from the Centre of Excellence "Severo Ochoa" award to the Instituto de Astrofísica de Canarias.

REFERENCES

- Almenara J. M., et al., 2022, *A&A*, **667**, L11
 Astropy Collaboration et al., 2013, *A&A*, **558**, A33
 Astropy Collaboration et al., 2018, *AJ*, **156**, 123
 Barclay T., Kostov V. B., Colón K. D., Quintana E. V., Schlieder J. E., Louie D. R., Gilbert E. A., Mullally S. E., 2021, *AJ*, **162**, 300
 Basri G., Shah R., 2020, *ApJ*, **901**, 14
 Batalha N. E., et al., 2017, *PASP*, **129**, 064501
 Bellm E. C., et al., 2019, *PASP*, **131**, 018002
 Berardo D., de Wit J., Rackham B. V., 2023, *arXiv e-prints*, p. [arXiv:2307.04785](https://arxiv.org/abs/2307.04785)
 Berdyugina S. V., 2005, *Living Reviews in Solar Physics*, **2**, 8
 Borucki W. J., et al., 2010, *Science*, **327**, 977
 Bradley L., et al., 2021, *astropy/photutils*: 1.3.0, Zenodo, [doi:10.5281/zenodo.5796924](https://doi.org/10.5281/zenodo.5796924)

- Brown T. M., et al., 2013, *PASP*, **125**, 1031
- Chambers K. C., et al., 2016, arXiv e-prints, p. [arXiv:1612.05560](https://arxiv.org/abs/1612.05560)
- Chang S. W., Byun Y. I., Hartman J. D., 2015, *ApJ*, **814**, 35
- Cracchiolo G., Micela G., Peres G., 2021, *MNRAS*, **501**, 1733
- Czesla S., Schröter S., Schneider C. P., Huber K. F., Pfeifer F., Andreasen D. T., Zechmeister M., 2019, PyA: Python astronomy-related packages (ascl:1906.010)
- Davenport J. R. A., et al., 2014, *ApJ*, **797**, 122
- Díaz R. F., Almenara J. M., Santerne A., Moutou C., Lethuillier A., Deleuil M., 2014, *MNRAS*, **441**, 983
- Edwards B., et al., 2021, *AJ*, **161**, 44
- Flewelling H. A., et al., 2020, *ApJS*, **251**, 7
- Foreman-Mackey D., 2016, *The Journal of Open Source Software*, **1**, 24
- Foreman-Mackey D., 2018, *Research Notes of the American Astronomical Society*, **2**, 31
- Foreman-Mackey D., Hogg D. W., Lang D., Goodman J., 2013, *PASP*, **125**, 306
- Foreman-Mackey D., Agol E., Ambikasaran S., Angus R., 2017, *AJ*, **154**, 220
- Fournier-Tondreau M., et al., 2024, *MNRAS*, **528**, 3354
- Frasca A., Covino E., Spezzi L., Alcalá J. M., Marilli E., Fűrész G., Gandolfi D., 2009, *A&A*, **508**, 1313
- Fukui A., et al., 2011, *PASJ*, **63**, 287
- Gaia Collaboration et al., 2016, *A&A*, **595**, A1
- Gaia Collaboration et al., 2023, *A&A*, **674**, A1
- Gaidos E., et al., 2020, *MNRAS*, **498**, L119
- Gardner J. P., et al., 2006, *Space Sci. Rev.*, **123**, 485
- Gressier A., Mori M., Changeat Q., Edwards B., Beaulieu J. P., Marcq E., Charnay B., 2022, *A&A*, **658**, A133
- Günther M. N., et al., 2020, *AJ*, **159**, 60
- Henry G. W., Eaton J. A., Hamer J., Hall D. S., 1995, *ApJS*, **97**, 513
- Herbst K., Papaioannou A., Airapetian V. S., Atri D., 2021, *ApJ*, **907**, 89
- Hunt-Walker N. M., Hilton E. J., Kowalski A. F., Hawley S. L., Matthews J. M., 2012, *PASP*, **124**, 545
- Husser T.-O., Wende-von Berg S., Dreizler S., Homeier D., Reiners A., Barman T., Hauschildt P. H., 2013, *A&A*, **553**, A6
- Ikuta K., et al., 2020, *ApJ*, **902**, 73
- Ikuta K., Namekata K., Notsu Y., Maehara H., Okamoto S., Honda S., Nogami D., Shibata K., 2023, *ApJ*, **948**, 64
- Irwin J. M., Berta-Thompson Z. K., Charbonneau D., Dittmann J., Falco E. E., Newton E. R., Nutzman P., 2015, in 18th Cambridge Workshop on Cool Stars, Stellar Systems, and the Sun. pp 767–772 ([arXiv:1409.0891](https://arxiv.org/abs/1409.0891))
- Jenkins J. M., 2002, *ApJ*, **575**, 493
- Jenkins J. M., et al., 2010, in Radziwill N. M., Bridger A., eds, Society of Photo-Optical Instrumentation Engineers (SPIE) Conference Series Vol. 7740, Software and Cyberinfrastructure for Astronomy. p. 77400D, [doi:10.1117/12.856764](https://doi.org/10.1117/12.856764)
- Jenkins J. M., et al., 2016, in Chiozzio G., Guzman J. C., eds, Society of Photo-Optical Instrumentation Engineers (SPIE) Conference Series Vol. 9913, Software and Cyberinfrastructure for Astronomy IV. p. 99133E, [doi:10.1117/12.2233418](https://doi.org/10.1117/12.2233418)
- Johnson L. J., Norris C. M., Unruh Y. C., Solanki S. K., Krivova N., Witzke V., Shapiro A. I., 2021, *MNRAS*, **504**, 4751
- Kain I. J., Newton E. R., Dittmann J. A., Irwin J. M., Mann A. W., Thao P. C., Charbonneau D., Winters J. G., 2020, *AJ*, **159**, 83
- Kass R. E., Raftery A. E., 1995, *Journal of the American Statistical Association*, **90**, 773
- Kipping D. M., 2012, *MNRAS*, **427**, 2487
- Kipping D. M., 2013, *MNRAS*, **435**, 2152
- Kreidberg L., 2015, *PASP*, **127**, 1161
- Lim O., et al., 2023, *ApJ*, **955**, L22
- Luger R., Foreman-Mackey D., Hedges C., Hogg D. W., 2021a, *AJ*, **162**, 123
- Luger R., Foreman-Mackey D., Hedges C., 2021b, *AJ*, **162**, 124
- Maehara H., Notsu Y., Notsu S., Namekata K., Honda S., Ishii T. T., Nogami D., Shibata K., 2017, *PASJ*, **69**, 41
- Mandel K., Agol E., 2002, *ApJ*, **580**, L171
- Mann A. W., et al., 2016, *ApJ*, **818**, 46
- Martín E. L., Lodieu N., Pavlenko Y., Béjar V. J. S., 2018, *ApJ*, **856**, 40
- Masci F. J., et al., 2019, *PASP*, **131**, 018003
- McCully C., Volgenau N. H., Harbeck D.-R., Lister T. A., Saunders E. S., Turner M. L., Siivervd R. J., Bowman M., 2018, in Guzman J. C., Ibsen J., eds, Society of Photo-Optical Instrumentation Engineers (SPIE) Conference Series Vol. 10707, Software and Cyberinfrastructure for Astronomy V. p. 107070K ([arXiv:1811.04163](https://arxiv.org/abs/1811.04163)), [doi:10.1117/12.2314340](https://doi.org/10.1117/12.2314340)
- Mendoza G. T., Davenport J. R. A., Agol E., Jackman J. A. G., Hawley S. L., 2022, *AJ*, **164**, 17
- Miyakawa K., Hirano T., Fukui A., Mann A. W., Gaidos E., Sato B., 2021, *AJ*, **162**, 104
- Moran S. E., et al., 2023, *ApJ*, **948**, L11
- Morris B. M., Agol E., Davenport J. R. A., Hawley S. L., 2018, *ApJ*, **857**, 39
- Murray C. A., et al., 2022, *MNRAS*, **513**, 2615
- Narita N., et al., 2019, *Journal of Astronomical Telescopes, Instruments, and Systems*, **5**, 015001
- Narita N., et al., 2020, in Society of Photo-Optical Instrumentation Engineers (SPIE) Conference Series. p. 114475K, [doi:10.1117/12.2559947](https://doi.org/10.1117/12.2559947)
- Norris C. M., et al., 2023, *MNRAS*, **524**, 1139
- Notsu Y., et al., 2013, *ApJ*, **771**, 127
- Panja M., Cameron R., Solanki S. K., 2020, *ApJ*, **893**, 113
- Parviainen H., Aigrain S., 2015, *MNRAS*, **453**, 3821
- Pinhas A., Rackham B. V., Madhusudhan N., Apai D., 2018, *MNRAS*, **480**, 5314
- Rackham B. V., de Wit J., 2023, arXiv e-prints, p. [arXiv:2303.15418](https://arxiv.org/abs/2303.15418)
- Rackham B., et al., 2017, *ApJ*, **834**, 151
- Rackham B. V., Apai D., Giampapa M. S., 2018, *ApJ*, **853**, 122
- Rackham B. V., et al., 2023, *RAS Techniques and Instruments*, **2**, 148
- Reid I. N., et al., 1991, *PASP*, **103**, 661
- Ricker G. R., et al., 2015, *Journal of Astronomical Telescopes, Instruments, and Systems*, **1**, 014003
- Rodrigo C., Solano E., 2020, in XIV.0 Scientific Meeting (virtual) of the Spanish Astronomical Society. p. 182
- Rodrigo C., Solano E., Bayo A., 2012, SVO Filter Profile Service Version 1.0, IVOA Working Draft 15 October 2012, [doi:10.5479/ADS/bib/2012ivoa.rept.1015R](https://doi.org/10.5479/ADS/bib/2012ivoa.rept.1015R)
- Rosich A., Herrero E., Mallonn M., Ribas I., Morales J. C., Perger M., Anglada-Escudé G., Granzer T., 2020, *A&A*, **641**, A82
- Stefansson G., et al., 2020, *AJ*, **160**, 192
- Thao P. C., et al., 2020, *AJ*, **159**, 32
- Thompson A., et al., 2024, *ApJ*, **960**, 107
- Tinetti G., et al., 2018, *Experimental Astronomy*, **46**, 135
- Tinetti G., et al., 2021, arXiv e-prints, p. [arXiv:2104.04824](https://arxiv.org/abs/2104.04824)
- Waalkes W., Berta-Thompson Z., Newton E., Mann A., Gao P., Wakeford H., Alderson L., Plavchan P., 2023, arXiv e-prints, p. [arXiv:2310.17043](https://arxiv.org/abs/2310.17043)
- Zechmeister M., Kürster M., 2009, *A&A*, **496**, 577
- Zhang M., Chachan Y., Kempton E. M. R., Knutson H. A., 2019, *PASP*, **131**, 034501

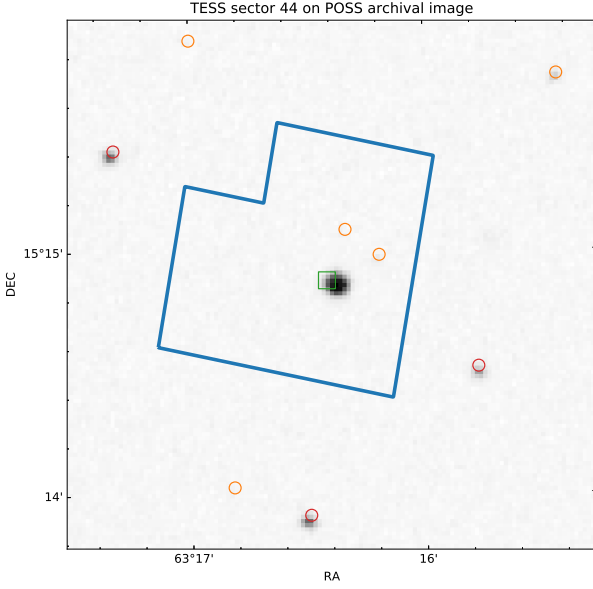


Figure A.1. Archival imaging from POSSII-F survey (Reid et al. 1991) with the TESS photometric aperture (blue outline) from Sector 44 and Gaia sources (red circles) from Gaia DR3 (Gaia Collaboration et al. 2016, 2023). The green square indicates the position of K2-25.

APPENDIX A: ADDITIONAL ANALYSES

A1 Analysis on the blended sources in the TESS photometry aperture

As K2-25 is located in a relatively crowded field, its photometric aperture of TESS could be contaminated by other sources. Since the blended sources can modify the observed brightness variability, we examined the effect of their contamination.

Figure A.1 shows the TESS photometric aperture of K2-25, overplotted with the archival field image. There are two faint Gaia sources (Gaia 3311804511206599168 and 3311804515501995648) in the aperture. Both of them are ~ 6 mag fainter than K2-25 in Gaia band (Gaia DR3; Gaia Collaboration et al. 2016, 2023), which means they contribute only $< 0.5\%$ of the measured flux. They can only change $\leq 1\%$ of the measured amplitude of the brightness variation, which is within the uncertainty of the amplitude measured with TESS (A.2). Therefore, we concluded that the effect of the blended sources is negligible.

A2 Another way to derive modulation amplitudes - Gaussian Process

To check the robustness of the results of the method presented in Section 3.2 (we call “sine-curve method” hereafter), we also obtained the brightness variation amplitudes of the five light curves in the following way, using the Gaussian process (GP). Assuming that the light curves are represented by a combination of periodic variations by the stellar rotation and white noise due to systematics, we used a combination of the modified quasi-periodic (MQP) kernel and the white-noise (WN) kernel in the Python package *celerite*:

$$k(\tau) = k_{\text{MQP}}(\tau) + k_{\text{WN}}(\tau) \quad (\text{A1})$$

$$k_{\text{MQP}}(\tau) = \frac{\theta_1}{2 + \theta_2} e^{-\tau/\theta_3} \left[\cos\left(\frac{2\pi\tau}{P}\right) + (1 + \theta_2) \right] \quad (\text{A2})$$

$$k_{\text{WN}}(\tau) = \theta_4 \delta(p, p'). \quad (\text{A3})$$

Table A.1. Priors and derived parameters for joint GP fit for the modulation analysis. $\mathcal{U}(X, Y)$ indicates the uniform prior which allows the range between X and Y .

Hyperparameter	Prior	Derived Value
P	1 (fix)	-
$\log \theta_1$ (Sinistro- g)	$\mathcal{U}(-15, 3)$	$-7.82^{+0.95}_{-0.77}$
$\log \theta_1$ (ZTF- g)	$\mathcal{U}(-15, 3)$	$-8.23^{+0.90}_{-0.79}$
$\log \theta_1$ (ZTF- r)	$\mathcal{U}(-15, 3)$	$-8.22^{+1.08}_{-0.99}$
$\log \theta_1$ (TESS)	$\mathcal{U}(-15, 3)$	$-9.82^{+0.79}_{-0.62}$
$\log \theta_1$ (Sinistro- z)	$\mathcal{U}(-15, 3)$	$-9.32^{+0.94}_{-0.84}$
$\log \theta_2$	$\mathcal{U}(-20, 5)$	$-10.6^{+6.2}_{-6.3}$
$\log \theta_3$	$\mathcal{U}(-10, 5)$	$-1.84^{+0.68}_{-0.83}$
$\log \theta_4$ (Sinistro- g)	$\mathcal{U}(-10, 0)$	-4.66 ± 0.14
$\log \theta_4$ (ZTF- g)	$\mathcal{U}(-10, 0)$	$-7.0^{+1.8}_{-2.0}$
$\log \theta_4$ (ZTF- r)	$\mathcal{U}(-10, 0)$	$-5.00^{+0.33}_{-0.74}$
$\log \theta_4$ (TESS)	$\mathcal{U}(-10, 0)$	$-6.621^{+0.067}_{-0.072}$
$\log \theta_4$ (Sinistro- z)	$\mathcal{U}(-10, 0)$	$-4.584^{+0.056}_{-0.054}$

Table A.2. Derived modulation amplitude for the five light curves, by sine-curve method and GP method.

Band	Amplitude (%)	
	Sine-curve method	GP method
Sinistro- g	4.16 ± 0.48	4.31 ± 0.54
ZTF- g	3.96 ± 0.69	3.75 ± 0.63
ZTF- r	2.98 ± 0.57	2.96 ± 0.51
TESS	1.954 ± 0.022	2.029 ± 0.055
Sinistro- z	2.00 ± 0.21	1.85 ± 0.23

Here, $\tau = |p - p'|$ is the difference of two data points at the stellar rotation phase p , and $\theta_1, \theta_2, \theta_3, \theta_4, P$ are the hyperparameters. θ_1 and θ_2 tune the strength of correlation between each observation point; θ_3 tunes the timescale of exponential decay; θ_4 accounts for the white noise level; P corresponds to period of the modulation.

We assumed the light curve is different only in the amplitude for each band, and the timescales of the decay are largely consistent in all bands. Therefore, we set θ_2 and θ_3 to be common parameters for all light curves, whereas θ_1 and θ_4 are different parameters for each light curve. Also, as the light curves are already phase-folded, we fixed the value $P = 1$. Therefore, we optimize the five light curves simultaneously, with 12 hyperparameters in total. We put log-uniform prior distributions for all the hyperparameters, which only prevent the hyperparameters from becoming too large and unphysical. We used MCMC package *emcee* for the parameter estimation. Parameters, priors, and derived values for each parameter are summarized in Table A.1.

Figure A.2 shows the resulted GP models plotted with the observed light curves. The amplitudes and their errors are derived by calculating the difference between the maximum and minimum values of the resulting light curve model with errors.

The derived amplitudes from the sine-curve method and the GP method are compared in Table A.2. The resulting posterior distribution of ΔT and f_{spot} is similar to the one by the sine-curve method. When adopting amplitude values from GP method, the median value and 2σ -upper limit of ΔT and f_{spot} was 68 K and 239 K, and 16% and 64%, respectively.

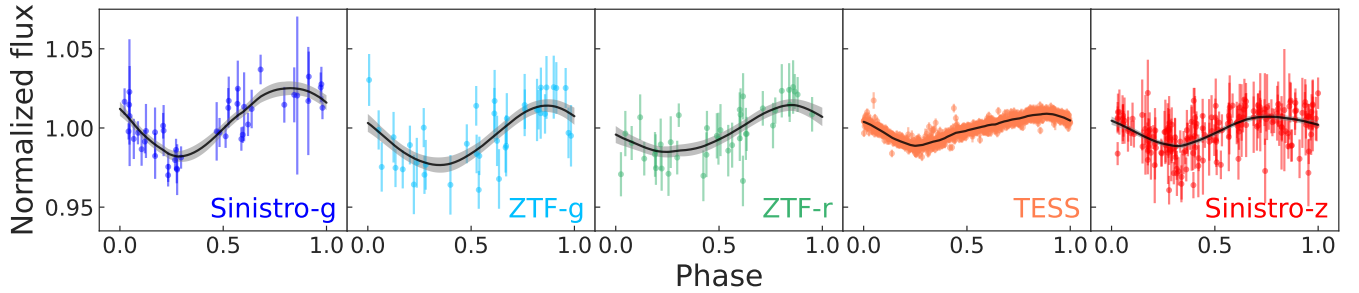


Figure A.2. The phase-folded light curves and fitted model curves by the GP method. The solid line shows the best-fit curves and the shaded region shows the 1σ uncertainties of the models. The white noise are taken into account by adding white noise kernels.

A3 Analysis on the long-term change of the variability amplitude

Kain et al. (2020) revealed that the modulation amplitude of K2-25 differs from year to year from the analyses of light curves observed with the MEarth Observatories (Irwin et al. 2015) over a three-year period. To see the recent long-term variation of the modulation amplitude, we divided the ZTF light curves into 8 different segments, each of which has a 200-day period and derived modulation amplitudes by the GP method. This time, the hyperparameters were fixed to the derived value described in Table A.1 for each ZTF band.

The shape of the brightness modulation is changing in a timescale of ~ 200 days, as shown in Figure A.3. The amplitude also varied at each time, with a relatively large amplitude during the period we observed with other instruments (MJD 59400 - 59800), and almost no visible variations during the previous period (MJD 59000 - 59400). In addition, the shape of the variation is consistent between Z_g and Z_r -band, with Z_g -band always showing a greater amplitude.

This means the spot distribution has changed in a timescale of a few $\times 100$ days, and it is difficult to constrain spot characteristics by the combination of different observations at the different observing epochs.

A4 Possibility of bright spots

In this section, we deal with the case of bright spots, which was not considered in the derivation of spot temperature and covering fraction from the brightness modulation amplitudes (Section 3.3). Bright spots can create similar modulations in light curves as described by Equation 3, although the bright spots are most visible when the star is brightest. We obtained a BT-Settl model with spot temperatures ranging from 3200 K to 5000 K in 100 K increments, which was interpolated for use.

Figure A.4 shows the resulting posterior distribution of spot characteristics from the modulation amplitudes. The derived values are $|\Delta T_{\text{spot}}| = 78^{+16}_{-11}$ K and $f_{\text{spot}} = 12 \pm 2\%$ with 1σ uncertainties.

The TLSE caused by those bright spots results in smaller transit depths in shorter wavelength in the optical. We calculated the chi-squared values of the calculated transit depths to observed transit depths as done in Section 4.4, adopting reasonable values for the bright spots case ($T_{\text{spot}} = 3300$ K and $f_{\text{spot}} = 15\%$). Table A.3 presents similar chi-squared values for all cases, which do not strongly suggest the existence of bright spots, considering the large errors in observed transit depths.

Here, bright spots refer to regions that have a higher temperature than the photosphere, and their physical characteristics are not con-

Table A.3. Similar to Table 5, but assuming $T_{\text{spot}} = 3300$ K and $f_{\text{spot}} = 15\%$.

Model	Data			
	(1)This Work		(2)This Work + T20	
	χ^2	reduced χ^2	χ^2	reduced χ^2
Flat with spot	5.22	1.31	15.4	1.71
Flat without spot	5.98	1.49	11.5	1.28
100 \times Solar with spot	4.93	1.23	25.6	2.84
100 \times Solar without spot	5.66	1.42	17.2	1.91

sidered. These could be faculae, but as explained in the Conclusion, faculae exhibit complex behaviour in light curves and are challenging to implement in spot mapping. This remains a future task, including how such regions, which slightly warmer than their surroundings, can be physically explained.

A5 Analysis on the transit depth variability

We analysed the transit depth variability to see if the TLSE causes the variability at the different stellar rotational phases.

Transit analysis was performed following the method described in Section 3.6. However, in this analysis, the transit depth was set as a separate parameter for each observation night, while the other transit parameters were common. Fitting was done for the four MuSCAT bands simultaneously. To reduce the computational cost, the GP hyperparameters were fixed with the best-fit values from the joint-fit results (Table 4). Therefore the total number of parameters was 36: T_0 , P , $\sqrt{e} \cos \omega$, $\sqrt{e} \sin \omega$, a/R_\star , b , and $(R_p/R_\star)_m$ for each light curve $m = \{1, 2, \dots, 22\}$, and (q_{1B}, q_{2B}) for each band $B = \{g, r, i, z\}$. Note that, since TESS transit data are not very high precision, we did not use them to examine transit depth variability in the first place.

Figure A.5 shows the derived transit depth variations in each band, along with the observing time and corresponding stellar rotational phase. The stellar rotational phase at each transit timing was calculated using the values of $P_{\text{rot}} = 1.87708$ day, described in Section 3.1.

At the same time, we calculated the degree of TLSE (contamination factor) ϵ_B at each band B per stellar rotation phase. In principle, the derivation of ϵ_λ (Equation 6) means the ratio of the ‘flux from the spotless stellar surface’ to the ‘flux from the current stellar surface’. This means that we can calculate the ϵ_B at each phase by dividing each phase-folded light curve by the maximum of the light curve. The dashed lines in Figure A.5 indicate the transit depth variation ex-

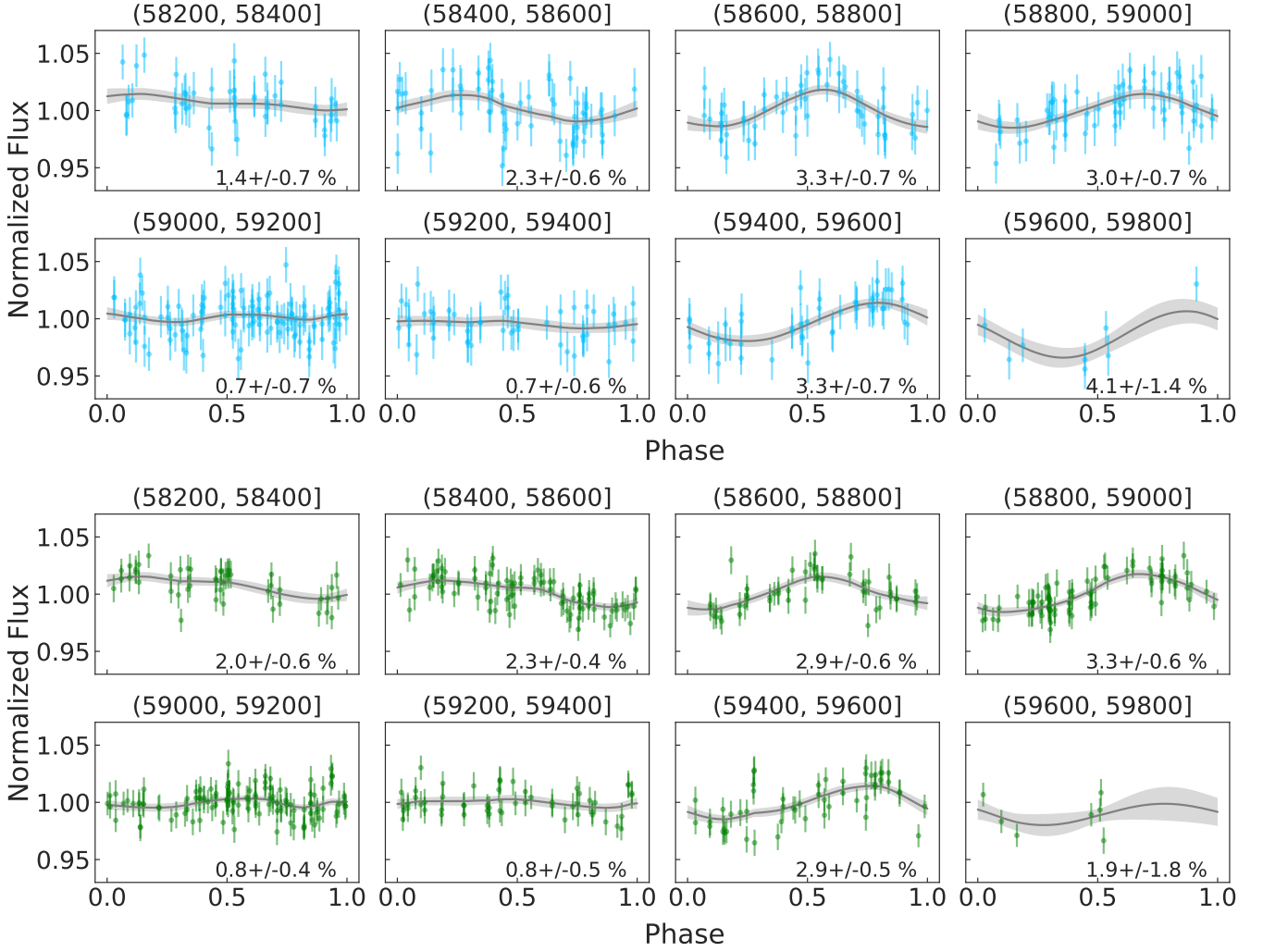


Figure A.3. (top) Phase-folded light curves in Z_g -band by ZTF, divided into 8 bins every 200 days, with GP model. The title of each panel shows the range of MJDs of the data used for that plot. (bottom) Same figure but for Z_r -band data. The shape of the brightness modulation is different in each bin.

pected from the TLSE. The predicted differences in transit depths are only < 500 ppm. This difference is not detectable with MuSCAT2/3 considering their photometric precision. This result was consistent with the result that transit depth was constant within the uncertainties.

A6 Analysis on the spot crossing probability

We investigate the possibility of spot-crossing events observed, as it gives useful information to constrain the spot characteristics. We did not visually detect any signal of large spot crossings from the shape of transit light curves, other than the suspicious signal observed in observation $N_T = 314$, which could not be determined whether it was spot-crossing or flare during transit. In another case, if there are many small spots on the transit chord, there should be random occurrences of those spots crossing during transits, which result in an increase in scatters during the transits when the light curves are stacked.

Therefore, we stacked the light curves in each band after GP detrending, as shown in Figure A.6. We also removed the transit signal from the light curves and calculated the RMS values of the residual, both in-transit and out-of-transit. The calculated RMS values are

Table A.4. Calculated RMS for the phase-stacked light curves in each band, after transit+baseline model correction.

Band	RMS	
	in-transit	out-of-transit
<i>g</i>	0.00590	0.00555
<i>r</i>	0.00347	0.00370
<i>i</i>	0.00218	0.00238
<i>z</i>	0.00278	0.00303
TESS	0.00599	0.00691

summarized in Table A.4. There is no significant increase in RMS in transit, indicating that there is no strong evidence of spot crossings.

The result is consistent with the fact that none of the transit observations by [Thao et al. \(2020\)](#) and [Kain et al. \(2020\)](#) gave a clear signal of spot crossings; one of the light curves by the Spitzer showed a signal that would be spot crossing, but the possibility of systematic error remains. These results suggest that the spots of K2-25 are not very large or not located at the transit chord.

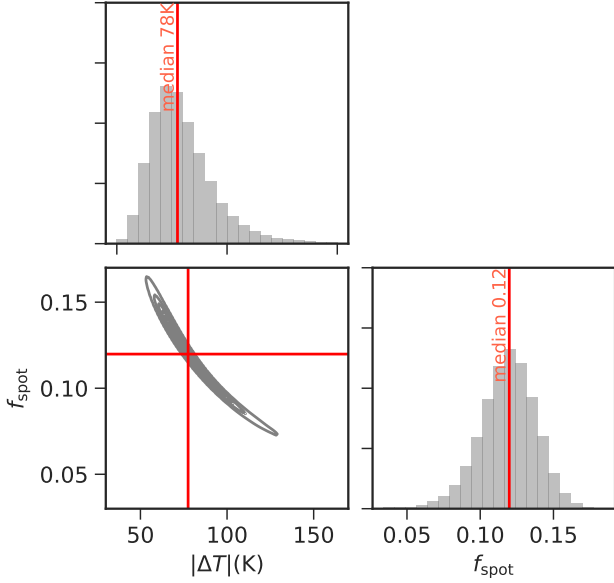


Figure A.4. Similar to Figure 5, but for the case of bright spots. The red lines represent the median values of the posterior distributions.

A7 Analysis on the flares from TESS light curve

From visual inspection, we found there are several flare-like signals in the TESS light curve. Frequent flares would not only lead to errors in transit depth measurements but would be another source of transit depth variations.

Therefore, we derived the flare frequency (how often flares of each energy occur) of the system, following the five steps; (1) detrending the light curves, (2) searching for flare candidates, (3) fitting flare models to the candidate light curve, (4) deriving total energy for each flare, and (5) deriving flare frequency.

First, we detrended the light curve. Assuming that the flares occur almost independently of the stellar rotation phase, models fitted to light curves folded in the stellar rotation phase can be regarded as unaffected by flares. Therefore, we detrended the TESS light curve by the phase-folded GP model described in Section 3.2 and unfolded it with time as the horizontal axis.

Second, the flare candidates were searched using the criteria described in Chang et al. (2015): “There are three or more consecutive points where the flux is more than 3σ off the overall median value”. As a result, three flare candidates were detected. We also visually checked all the other data points that exceed 3σ from the median and did not confirm flare-like signals other than these three. Figure A.7 shows the normalized TESS light curves, with and without detrending, along with the times of three detected flare candidates.

We cut out a light curve at 0.02 days before and 0.08 days after the first rise of each flare-like signal. To model the flare light curves, we used the empirical flare template Llamardas Estelares (Mendoza et al. 2022), which is an updated model from Davenport et al. (2014). The flare shape in the light curves $F_{\text{flare}}(t)$ is characterized by three parameters: the time of flare peak t_{peak} , the time-scale of decay FWHM, and the peak amplitude of the flux f_{amp} . Independently for each flare candidate, parameter estimation was performed by emcee to maximise the likelihood of the flare model to the observed flare light curve. The emcee chain was well-converged, indicating that the probability that these are typical flares is high.

Therefore, the equivalent duration (ED) of the flare and flare energy

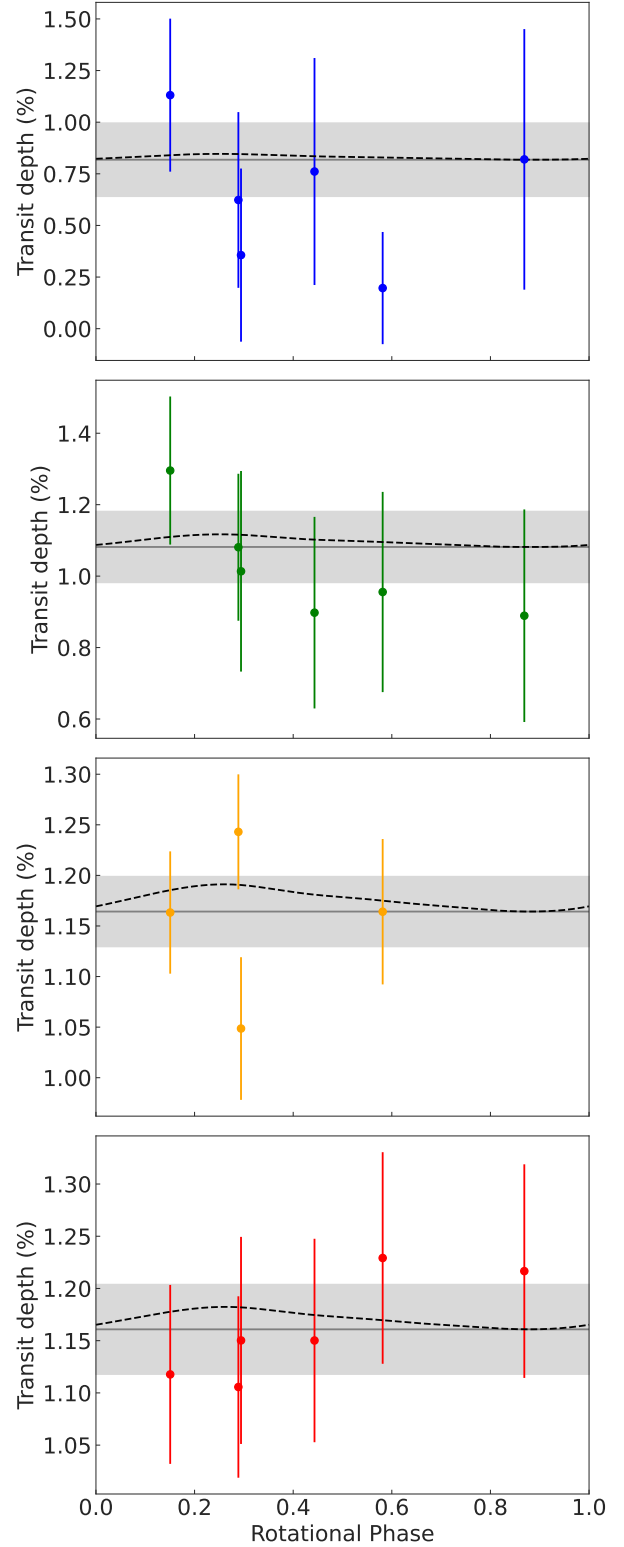


Figure A.5. Derived transit depths according to the stellar rotation phase for g , r , i , and z -band from the top to the bottom. The grey lines and regions show the transit depths and their uncertainties derived by joint fit. The black dashed lines show the predicted transit depth variation from the TLSE. The derived uncertainties in the transit depths are larger than the predicted transit depth variation.

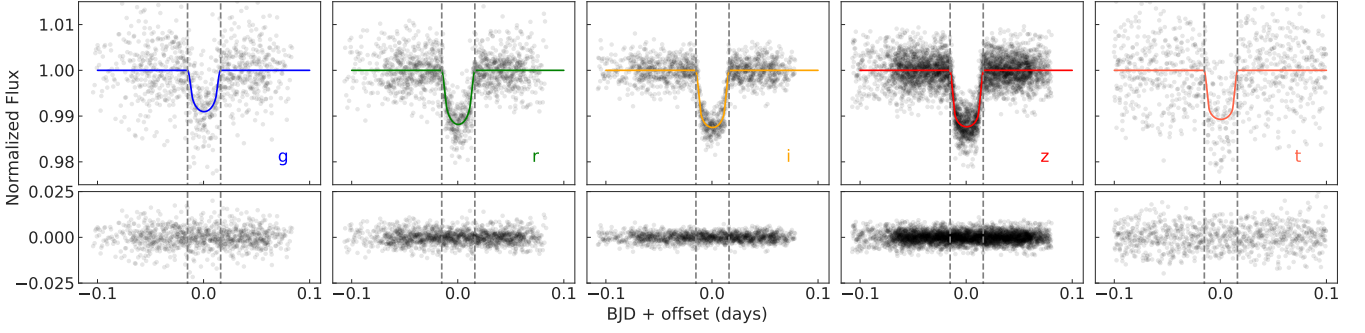


Figure A.6. (Top) Best-fit transit models and observed data points phase-folded at the planetary orbital period after correcting baseline modulation. (Bottom) Residuals after subtracting the transit and baseline models from the observed data. There are no signs of spot crossings that would cause a larger RMS in transit.

at the observed band E_{flare} were calculated from the flare flux variation $F_{\text{flare}}(t)$, by the following equations described in [Hunt-Walker et al. \(2012\)](#).

$$ED = \int \frac{F_{\text{flare}}(t)}{F_0} dt, \quad (\text{A4})$$

$$E_{\text{flare}} = L_{\star} \times ED, \quad (\text{A5})$$

where F_0 is the quiescent stellar flux and L_{\star} is the stellar luminosity in the observed band. We calculated ED and E_{flare} from $F_{\text{flare}}(t)/F_0$ as the best-fit normalized model and $L_{\star} = 0.00816L_{\odot} = 3.12 \times 10^{31}$ erg/sec from [Thao et al. \(2020\)](#). Figure A.8 shows the light curves of three detected flares with the model curve, and calculated ED and E_{flare} . Calculated flare energy values are $\sim 3 \times 10^{33}$ erg, 2×10^{33} erg, and 1×10^{33} erg for three flares, respectively.

Although the number of flares detected is small, flare frequency was roughly estimated. The observation period of the TESS light curve was 21.76 days, not including the gap for data downlink. Within this observing window, we found three flares with the energy at $\sim 10^{33}$ erg and did not find flares with higher energy. We estimate the $\sim 10^{33}$ erg-class flare happens ~ 0.1 per day. The smaller flares should happen more frequently, but they seem to be below the detection limit ($\sim 10^{32}$ erg).

Such flares can affect the accurate measurement of transit depths. Indeed, our transit light curves by MuSCAT2/3 showed flare-like brightening during the transit observations (Figure A.9). We did not model the flare in the transit analysis, as the observational precision is not that high compared to the flare amplitude. The influence of the flare on the transit depth measurement should have been suppressed by removing outliers and using a Gaussian process as a noise model. However, in the future, when more precise transit observations are made by space telescopes, attention should be paid to whether flares are occurring during, before, or after the transit.

A8 Analysis on the effectiveness of multi-band monitoring

To confirm the effectiveness of multi-band monitoring observations for spot characteristics derivation, we tried the spot mapping analysis described in Section 3.4 only using the TESS light curve, to compare with the result using all five light curves.

Figure A.10 compares the resulted best-fit light curve models and their 1σ uncertainties, and Figure A.11 shows the posterior distribution of spot parameters for a three-spot model, which compares the result of TESS-only light curve v.s. five-band light curves. When only the TESS light curve was used, the MCMC did not converge with the reasonable iteration steps. Therefore, we needed to put additional

Gaussian prior for three parameters that describe the spot longitudes, and a uniform prior for ΔT to take values between 0 to 500 K, for the TESS-only case. Nevertheless, the five-band light curve case resulted in more strict constraints on the models and posterior distribution of spot parameters. Especially, while the TESS-only case allows spot latitude to be high (intuitively, to create a more smoothly modulating light curve), the spot latitudes are more constrained to be ~ 40 deg in the five-band light curve case. This resulted in a better constraint on spot temperature, by reflecting the correlations between spot parameters. The 2σ upper limit of ΔT was 407 K when only the TESS light curve is used, compared with the 86 K when five-band light curves are used. The results show that the light curves from ground-based telescopes, which have lower time coverage and photometric precision compared to the TESS light curve, still work toward reducing the model uncertainties.

This paper has been typeset from a $\text{\TeX}/\text{\LaTeX}$ file prepared by the author.

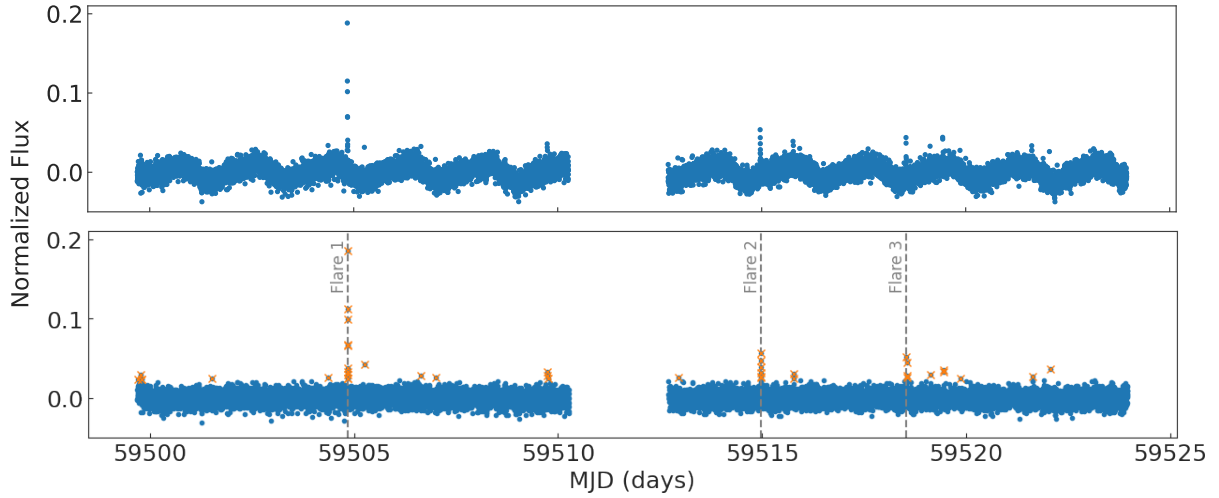


Figure A.7. Normalized PDCSAP light curve of K2-25 from TESS Sector 44 (top) and the detrended light curve by phase-folded GP model (bottom). Data points whose normalized flux values are more than 3σ away from the median value of the entire detrended curve are marked with orange crosses. The flare candidates are indicated by the grey dotted lines.

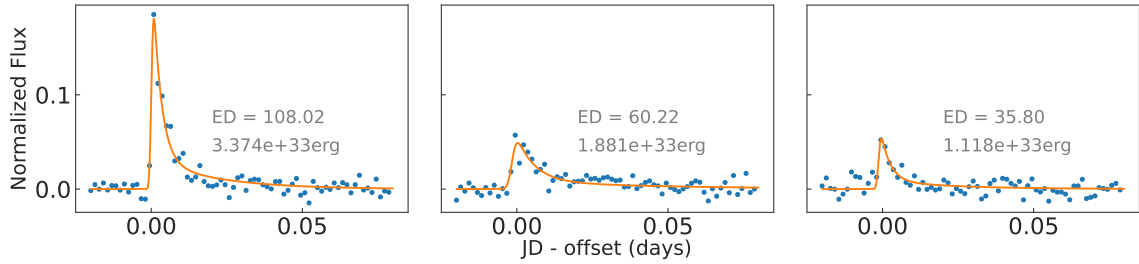


Figure A.8. Close-up of the light curves of visually selected flare candidates (flare 1 to 3, from left to right). The orange line shows the best-fit flare models. Calculated equivalent duration (ED) and flare energy are shown next to the models.

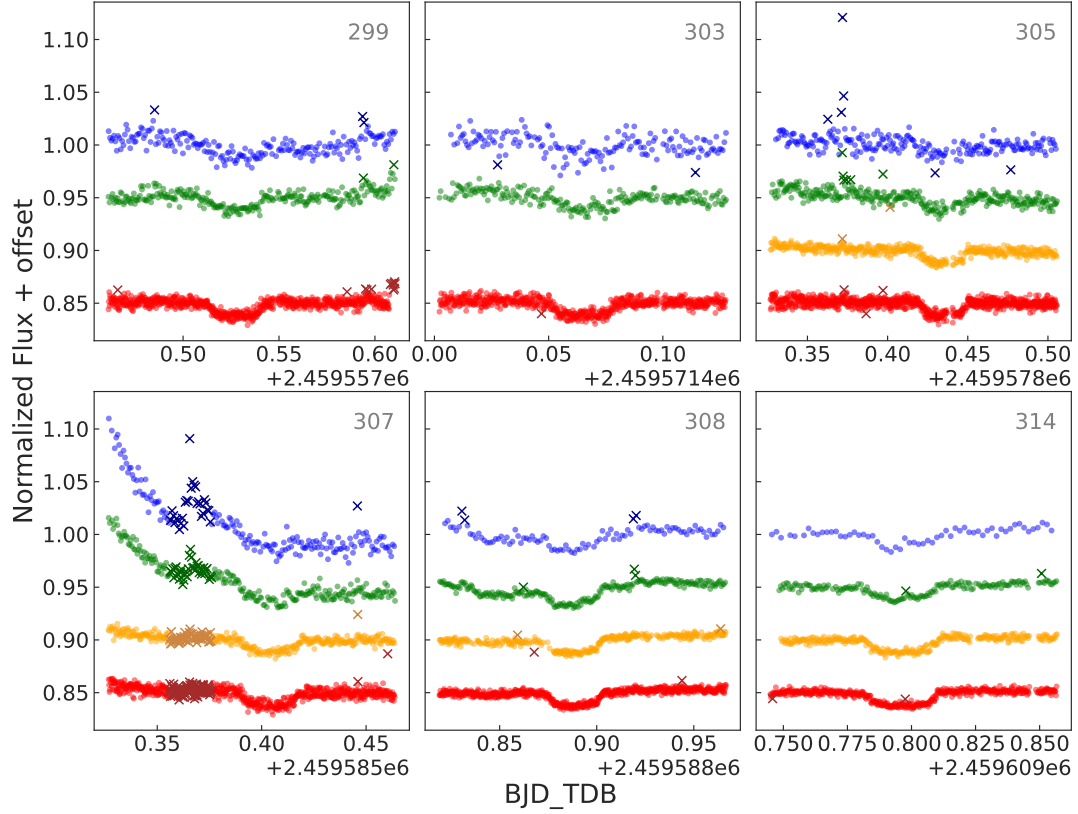


Figure A.9. Raw light curves by MuSCAT2/3 before removing outliers, in g , r , i , z -band from top to bottom at each panel, at each night. The coloured dots indicate the data points used for transit analysis, and cross marks indicate the removed data points. The values at the upper-right corner of each panel indicate the N_T values. There are several flare-like signals detected and removed as outliers. The details of outlier removal are described in Section 2.4.

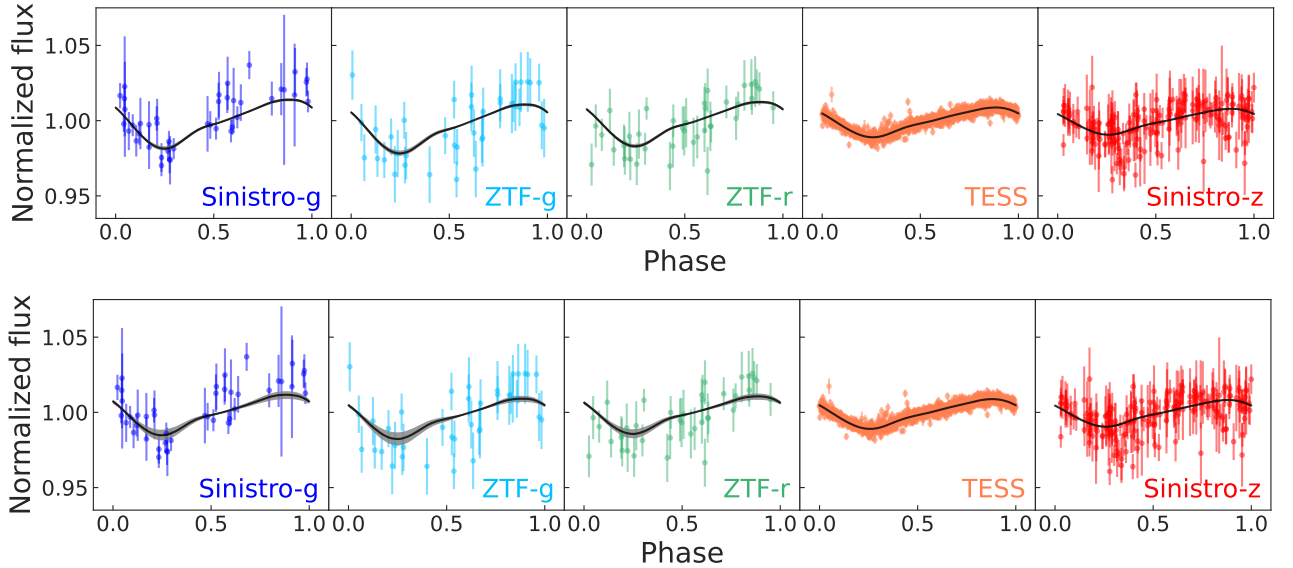


Figure A.10. (Top.) The phase-folded light curves and fitted model curves derived by the spot mapping with the three-spot case. The solid line shows the best-fit curves and the shaded region shows a 1σ deviation of model uncertainties, derived from the models drawn from the converged MCMC chain of the spot parameters. (Bottom.) As a comparison, a result of model fitting when only TESS light curves are used. Light curves are more well-constrained when we use multi-band light curves.

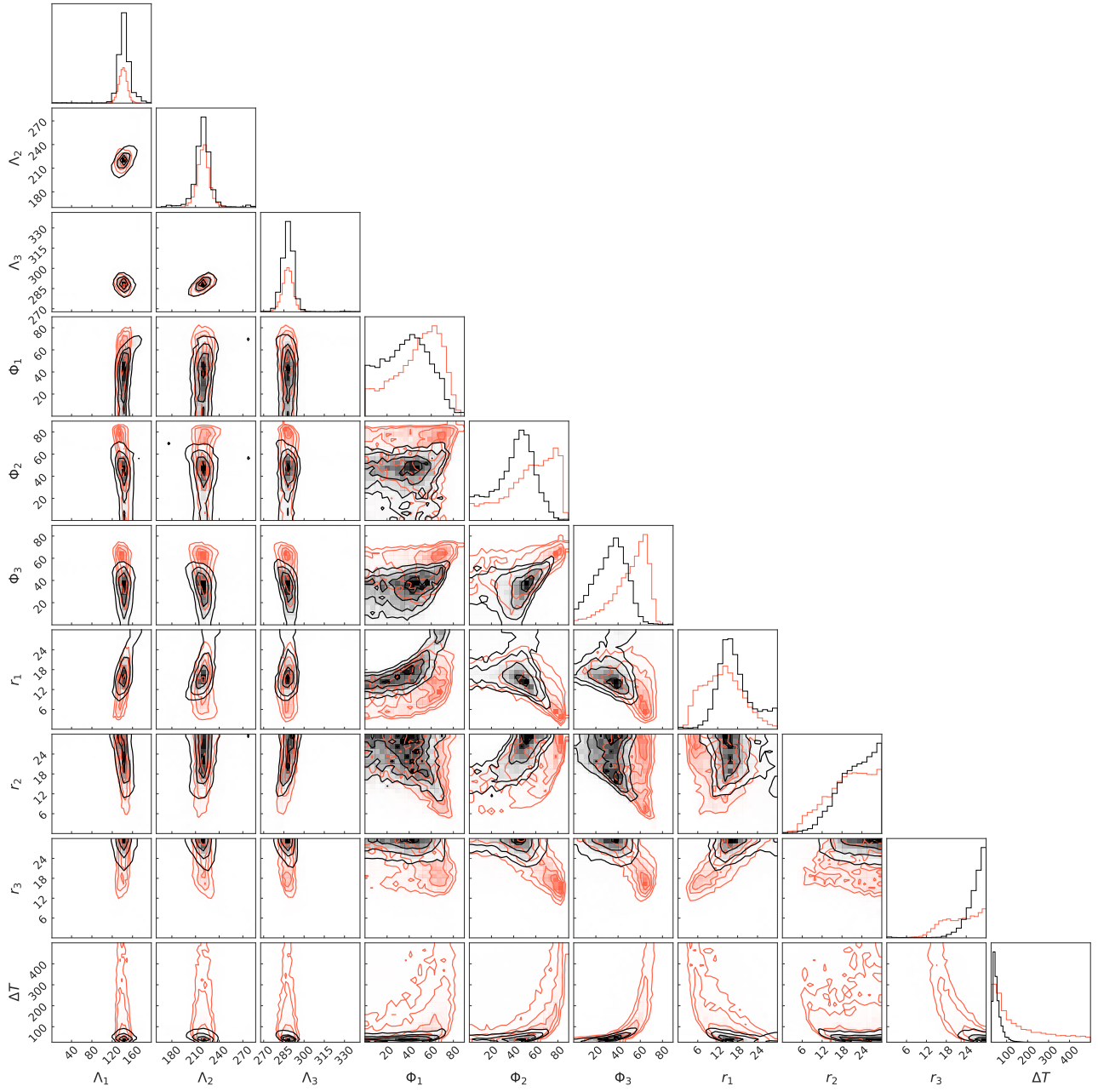


Figure A.11. Corner plot to show the posterior distribution of parameters for spot mapping using all five light curves (black) overlaid with the posteriors using only TESS light curve (orange); spot longitude Λ_n , latitude Φ_n and spot radius r_n for spot $n = \{1, 2, 3\}$ with three spot assumption. In the multi-band case, the spot latitudes are more limited not to reach higher values, thereby the spot temperature is more strongly constrained.